Supplementary Information

for

Ag_2S Monolayer: an Ultrasoft Inorganic Lieb Lattice

Tong Yang,†[a] Yong Zheng Luo,†[a] Zishen Wang,[a] Tao Zhu,[a] Hui Pan,[b] Shijie Wang,[c] Shu Ping Lau,[d] Yuan Ping Feng*[a] and Ming Yang*[d]

[a] Department of Physics, National University of Singapore, Singapore 117542, Singapore.

[b] Institute of Applied Physics and Materials Engineering, University of Macau, Macao SAR 999078, P. R. China.

[c] Institute of Materials Research & Engineering, A*STAR (Agency for Science, Technology and Research), 2 Fusionopolis Way, Innovis, Singapore 138634, Singapore.

[d] Department of Applied Physics, the Hong Kong Polytechnic University, Hung Hom, Hong Kong, P. R. China.

† Tong Yang and Yong Zheng Luo contributed equally to this work.

* To whom correspondence should be addressed: M. Y. (mingyang@polyu.edu.hk); Y. P. F. (phyfyp@nus.edu.sg).

This file includes:

Computational details

All first-principles calculations were performed using the Vienna *ab initio* simulation package (VASP).[1, 2] The projector wave-augmented method and the Perdew-Burke-Ernzerhof parameterized generalized gradient approximation were used to describe the core-electron interaction and the exchange-correlation interaction, respectively.[3-5] The electronic wave function was expanded in a plane wave basis with a cutoff kinetic energy of 455 eV. The convergence threshold for the total energy was set to 1.0×10^{-6} eV. For geometrical optimizations, both the lattice parameters and the atomic coordinates were fully optimized until the force acting on each atom less than 5 meV/Å. The Γ-centered Monkhorst-Pack schemed *k*-mesh was adopted to sample the first Brillouin zone in such a way that $a_i k_i \approx 53$, where a_i and k_i are the in-plane lattice constant and the number of subdivisions along the corresponding reciprocal lattice vector *i*, respectively. Along the out-of-plane direction, a vacuum layer of around 20 Å was inserted to eliminate the spurious interaction between layers. The phonon calculations were performed based on a $5 \times 5 \times 1$ Ag_2S supercell using the finite displacement method as implemented in the PHONOPY code.[6]

The particle swarm optimization algorithm as implemented in the CALYPSO code was deployed to search for the ground-state structure of 2D Ag_2S.[7-9] Unit cells containing 4 formula units (f.u.) of Ag_2S, namely Ag_8S_4, were considered. The number of generations was set to 30. In the first generation, 30 2D Ag_8S_4 structures were randomly generated and geometrically optimized using VASP. Among these optimized structures, 70 % of the lowest-energy structures were selected as parent structures and evolved into the next generation, whereas the other 30 % of the Ag_8S_4 structures in the next generation were randomly generated. Considering the intensive computational cost, the cutoff kinetic energy of the plane wave basis for electronic wave function expansion was reduced to 400 eV. The convergence criterion for the total energy and the geometric optimization was relaxed to 2×10^{-4} eV and 2×10^{-3} eV, respectively. The *k*-mesh was reduced to $a_i k_i \approx 13$.The identified lowest-energy 2D Ag_2S structures were further optimized using the tighter calculation setup mentioned above.

Tight-binding model

The basis set of the tight-binding model is $\{\phi_S(\vec{r}),\ \phi_{Ag_1}(\vec{r}),\ \phi_{Ag_2}(\vec{r})\}$ in the real space, where $\phi_i(\vec{r})$ is the localized wavefunction centred at site $i = S,\ Ag_1,\ Ag_2$, as shown in **Figure 1a**. $\phi_S(\vec{r})$ is mainly composed of the S-*p* orbitals, whereas $\phi_{Ag_1}(\vec{r})$ and $\phi_{Ag_2}(\vec{r})$ are mainly made up of the Ag-d_{xy}, $d_{x^2-y^2}$ orbitals (see **Figure 2**). In momentum space, Eq. (1) becomes $H_0 = \sum_{\vec{k}} \Psi_{\vec{k}}^{\dagger} H_0(\vec{k}) \Psi_{\vec{k}}$, where $\Psi_{\vec{k}} = \left(c_{S\vec{k}}, c_{Ag_1\vec{k}}, c_{Ag_2\vec{k}}\right), \vec{k} = (k_1, k_2)$ and

$$H_0(\vec{k}) = \begin{pmatrix} E_{00} & E_{01} & E_{02} \\ E_{01}^{*} & E_{11} & E_{12} \\ E_{02}^{*} & E_{12}^{*} & E_{22} \end{pmatrix} \quad (S1)$$

$$E_{00} = \epsilon_S$$

$$E_{01} = 2t_1 \cos\left(\frac{a}{2}k_1\right)$$

$$E_{02} = 2t_1 \cos\left(\frac{a}{2}k_2\right)$$

$$E_{11} = \epsilon_{Ag} + 2t_3 \cos\left(ak_2\right) + 2t_4 \cos\left(ak_1\right)$$

$$E_{12} = 4t_2 \cos\left(\frac{a}{2}k_1\right) \cos\left(\frac{a}{2}k_2\right)$$

$$E_{22} = \epsilon_{Ag} + 2t_3 \cos\left(ak_1\right) + 2t_4 \cos\left(ak_2\right)$$

where $a = |\vec{a}_1| = |\vec{a}_2|$ is the lattice constant of the planar Lieb lattice (see **Figure 1a**). If the NNN spin-orbit coupling interaction in Eq. (2) is taken into account, the Hamiltonian reads

$$H(\vec{k}) = \begin{pmatrix} H_0 + H_{SOC} & 0 \\ 0 & H_0 + H_{SOC}^{\dagger} \end{pmatrix} \quad (S2)$$

$$H_{SOC}(\vec{k}) = \begin{pmatrix} 0 & 0 & 0 \\ 0 & 0 & -4i\lambda \sin\left(\frac{a}{2}k_1\right) \sin\left(\frac{a}{2}k_2\right) \\ 0 & 4i\lambda \sin\left(\frac{a}{2}k_1\right) \sin\left(\frac{a}{2}k_2\right) & 0 \end{pmatrix}$$

Due to the spin degeneracy, we will restrict ourselves to the spin-up part of the Hamiltonian. The TB bands given by the Hamiltonian Eq. (S1) and Eq. (S2) are fitted to CB-II, VB-I and VB-II of

the calculated DFT bands at the PBE and HSE06 level. The TB bands match well with the DFT bands around the Brillouin zone centre as shown in **Figures 3** and **S18**. The fitted parameters are summarized in **Table S2**.

At the $M_{u.c.}^{'}$ point, the eigen-energies of the Hamiltonian are calculated to be

$$E_1\left(M_{u.c.}^{'}\right) = \epsilon_S \quad (S3)$$

$$E_2\left(M_{u.c.}^{'}\right) = \epsilon_{Ag} - 2t_3 - 2t_4 + 4|\lambda| \quad (S4)$$

$$E_3\left(M_{u.c.}^{'}\right) = \epsilon_{Ag} - 2t_3 - 2t_4 - 4|\lambda| \quad (S5)$$

One can see that the double degeneracy at $M_{u.c.}^{'}$ point (VBM) can only be lifted by the SOC interaction, which is observed in our DFT calculations (**Figures 2a** and **S22**). In addition, the energy gap between the two Dirac bands (CB-II and VB-II) at the $M_{u.c.}^{'}$ point can be written as

$$\Delta E\left(M_{u.c.}^{'}\right) = E_1\left(M_{u.c.}^{'}\right) - E_3\left(M_{u.c.}^{'}\right) = \epsilon_S - \epsilon_{Ag} + 2t_3 + 2t_4 + 4|\lambda| \quad (S6)$$

Since $\epsilon_S - \epsilon_{Ag}$ is much larger than t_3, t_4 and λ (see **Table S2**), the energy gap is mainly contributed by the difference in the local electronic potential between the S and Ag sites (see **Figure S19a**).

Along the $M_{u.c.}^{'} - X_{u.c.}^{'}$ k-path, along which the electronic states are folded to along the $\Gamma - M_{\sqrt{2}}$ k-path of the reduced 1BZ of Ag_2S (**Figure 3a**), the Hamiltonian in Eq. (2) is reduced to

$$H_0\left(M_{u.c.} - Y_{u.c.}\right) = \begin{pmatrix} \epsilon_S & 2t_1\cos\left(\frac{a}{2}k_1\right) & 0 \\ 2t_1\cos\left(\frac{a}{2}k_1\right) & \epsilon_{Ag} - 2t_3 + 2t_4\cos\left(ak_1\right) & 0 \\ 0 & 0 & \epsilon_{Ag} + 2t_3\cos\left(ak_1\right) - 2 \end{pmatrix}$$

Clearly, the Hamiltonian is independent of the NNN interaction (t_2). Instead, the TNN_H (t_3) and TNN_S (t_4) interactions play key roles in determining the band dispersion of VB-I and VB-II along the $M_{u.c.}^{'} - X_{u.c.}^{'}$ ($\Gamma - M_{\sqrt{2}}$) k-path. As shown in **Figure S19**, the TNN_H interaction determines the dispersion of VB-I along the $\Gamma - M_{\sqrt{2}}$ ($M_{u.c.}^{'} - X_{u.c.}^{'}$) direction, whereas the TNN_S interaction contributes to the dispersion of VB-II. Along the $\Gamma - X_{\sqrt{2}}$ ($M_{u.c.}^{'} - Q_{u.c.}^{'}$), on the other hand, **Figure S19** shows that both the NNN (t_2) and TNN (t_3 and t_4) interaction contribute to the valence band dispersion.

Topological characterization

The topological invariants and edge states of the Lieb-lattice Ag_2S were calculated based on the Wannier functions (WFs) which were established using the Ag-s, Ag-d, S-s and S-p orbitals as the initial guess for the unitary transformations.[10, 11] Due to the spin degeneracy and conservation of S_z, the topological invariants of the Lieb-lattice Ag_2S can be characterized by spin Chern number $C_n^S = (C_{n\uparrow} - C_{n\downarrow})/2$, where $C_{n\sigma}$ is the Chern number of the *n*th band of spin σ ($\sigma = \uparrow, \downarrow$). It can be calculated by integrating the Berry curvature over the whole BZ (Ω_n):[12]

$$C_n = \frac{1}{2\pi}\int_{BZ} \Omega_n(\vec{k}) d^2\vec{k} \quad (S8)$$

$$\Omega_n(\vec{k}) = -2Im \sum_{m \neq n} \frac{\langle \Psi_{n\vec{k}} | v_x | \Psi_{m\vec{k}} \rangle \langle \Psi_{m\vec{k}} | v_y | \Psi_{n\vec{k}} \rangle}{(\varepsilon_{n\vec{k}} - \varepsilon_{m\vec{k}})^2} \quad (S9)$$

$\Psi_{n\vec{k}}$ and $\varepsilon_{n\vec{k}}$ are the eigenstate and eigenvalue of the *n*th band at $\vec{k}$, respectively. v_x and v_y are the velocity operators.

Based on a recursive strategy,[13] the iterative Green's function of the semi-infinite lattice was constructed from the WFs to visualize the edge states.[14] The edge states were obtained by calculating the edge density of states within a semi-infinite system which was built by a truncation along the $\Gamma - M_{\sqrt{2}}$ direction to remove the periodicity along the $X - X$ direction.

The buckling height-dependent total energy of the Lieb-lattice Ag_2S

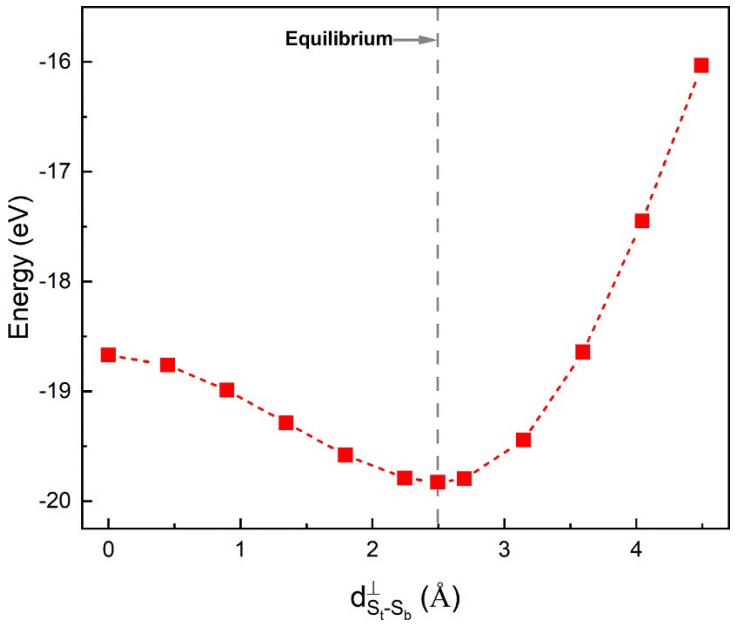

Figure S1. The total energy of the Lieb-lattice Ag_2S as a function of the buckling height ($d_{S_t}{}^{\perp}{}_{S_b}$).

The eight lowest-energy 2D Ag_2S structures predicted by CALYPSO

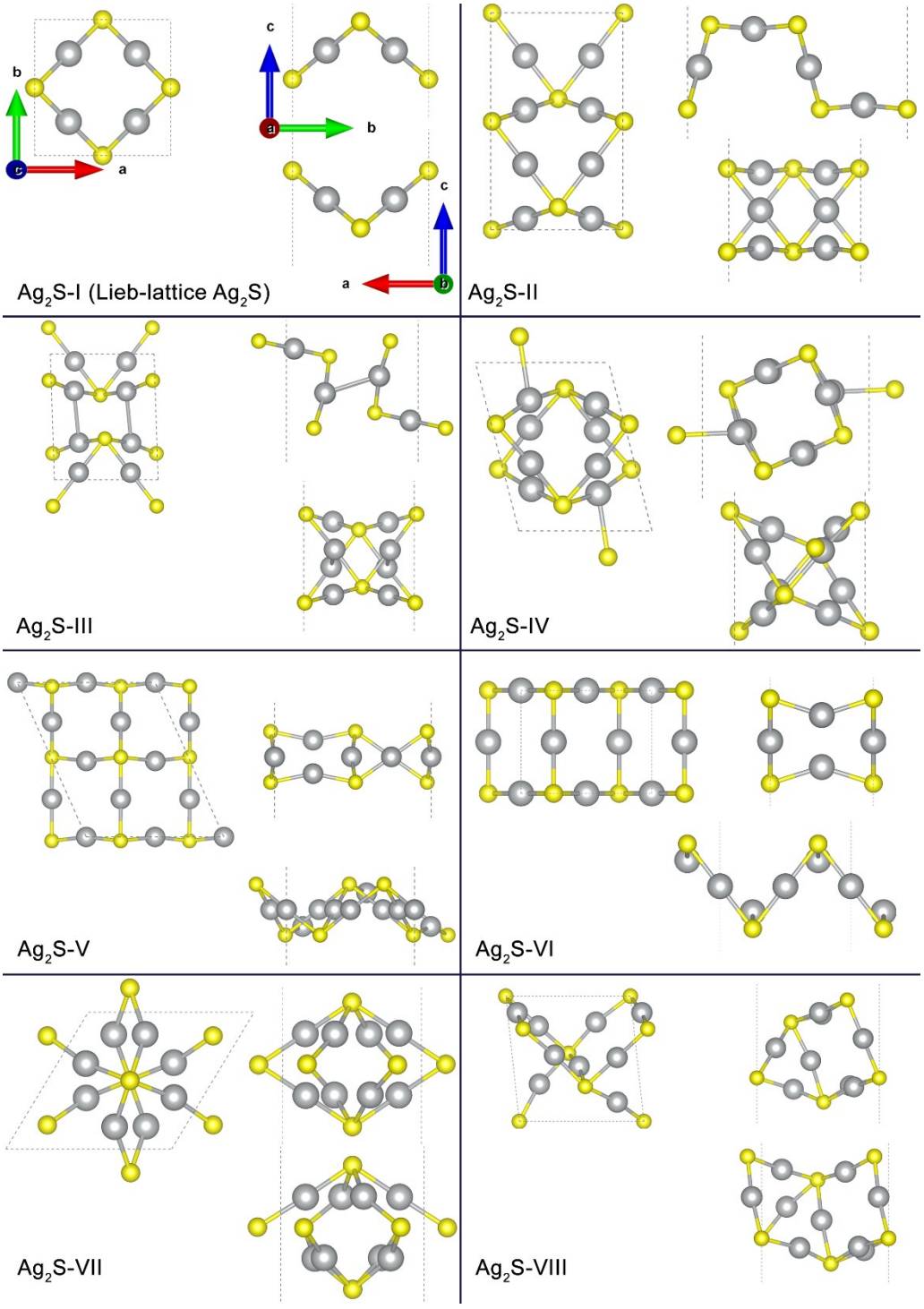

Figure S2. Schematic illustration of the most energetically stable structures of Ag_2S predicted by CALYPSO. They are relaxed at the PBE level and labelled in an ascending order of energy (E).

Table S1. The energy (*E*), the optimized in-plane lattice constants (*a* and *b*) and the lattice angle (γ), the space group and work function (E_{wf}) of the eight lowest-energy states of 2D Ag_2S calculated using the PBE functional and the PBE functional with the DFT-D3 correction. *E* is normalized to 2 formula units, *i.e.,* Ag_4S_2. The number in the parentheses in the space group column is the associated international table number.

	Ag_2S-	*E* (eV)	*a* (Å)	*b* (Å)	γ (°)	space group	E_{wf} (eV)
PBE	I	-19.828	5.906	5.906	90	$P42_12$ (90)	5.811
	II	-19.819	5.911	9.719	90	$Pmc2_1$ (26)	5.827
	III	-19.779	5.877	7.136	91.834	*P*-1 (2)	5.771
	IV	-19.770	5.875	7.682	104.449	*P*-1 (2)	5.814
	V	-19.729	7.784	9.563	113.949	*P*12/*c*1 (13)	5.854
	VI	-19.635	6.579	4.686	90	*Pmma* (51)	5.711
	VII	-19.537	7.184	6.928	58.941	*P*1 (1)	5.372
	VIII	-19.413	6.772	6.855	96.148	*P*1 (1)	5.779
PBE+DFT-D3	I	-20.951	5.806	5.806	90	$P42_12$ (90)	5.751
	II	-21.238	5.792	6.250	90	*Pbcm* (57)	5.409
	III	-21.369	5.784	6.831	90.641	*P*-1 (2)	5.636
	IV	-21.313	5.801	7.566	112.506	*P*-1 (2)	5.679
	V	-20.854	7.376	9.361	113.180	*Cmma* (67)	5.804
	VI	-20.814	6.001	4.651	90	*Pmma* (51)	5.621
	VII	-21.161	6.979	6.800	59.265	*P*1 (1)	5.354
	VIII	-21.040	6.619	5.785	88.687	*P*1 (1)	5.524

To estimate the effect of the Van der Waals (vdW) interaction, we adopted the DFT-D3 method (PBE+DFT-D3)[15, 16]. From **Table S1**, it is found that the vdW interaction indeed has a pronounced impact on the energetics of the eight lowest-energy structures. Nevertheless, the Lieb-lattice Ag_2S (Ag_2S-I) considered in the present study is consistently lower in energy than the recently reported α-Ag_2S monolayer (Ag_2S-VI)[17], *i.e.*, 32 meV/atom for PBE and 23 meV/atom for PBE+DFT-D3.

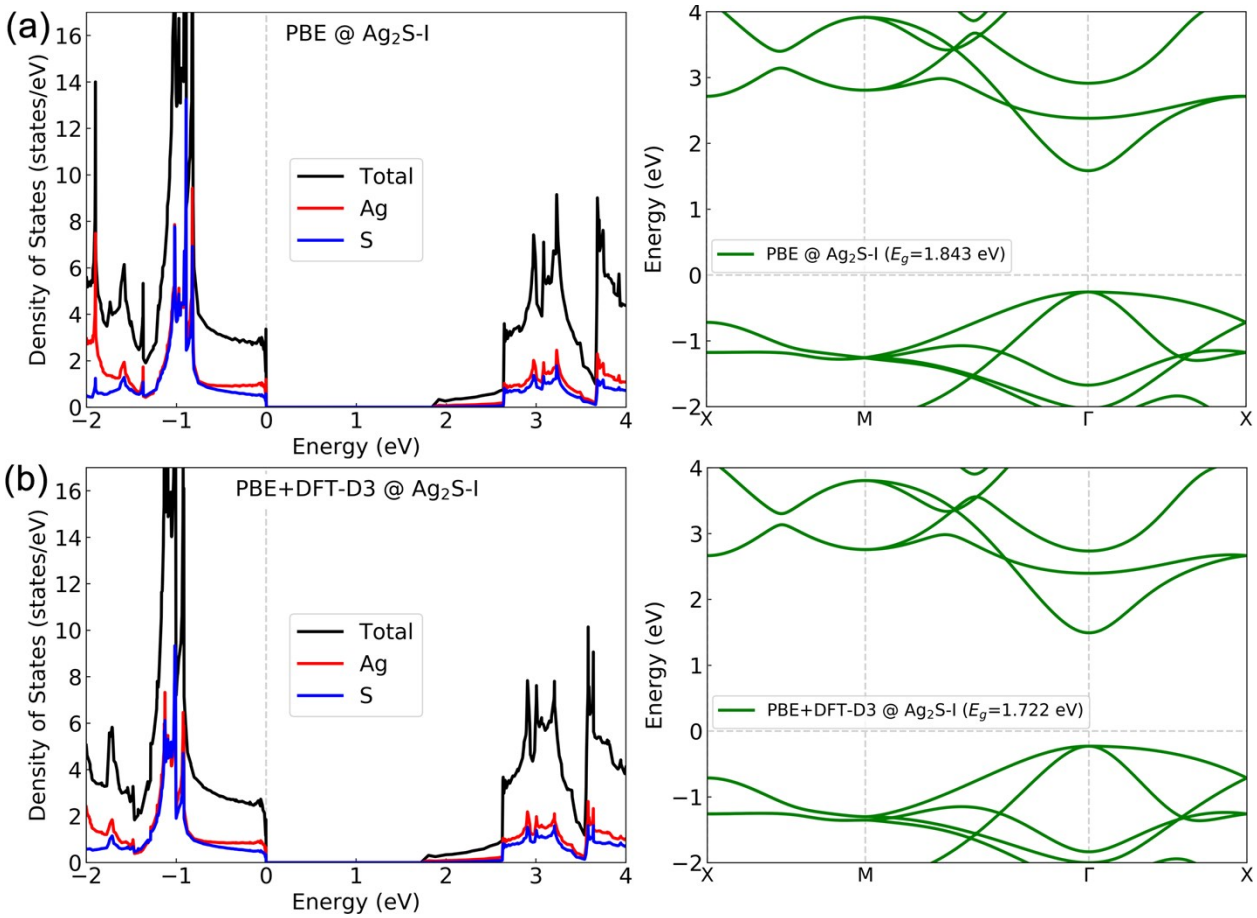

Figure S3. The density of states (DOS) (left panel) and the electronic band structure (right panel) of Ag_2S-I (Lieb-lattice Ag_2S) calculated using (a) the PBE functional and (b) the PBE functional with the DFT-D3 correction.

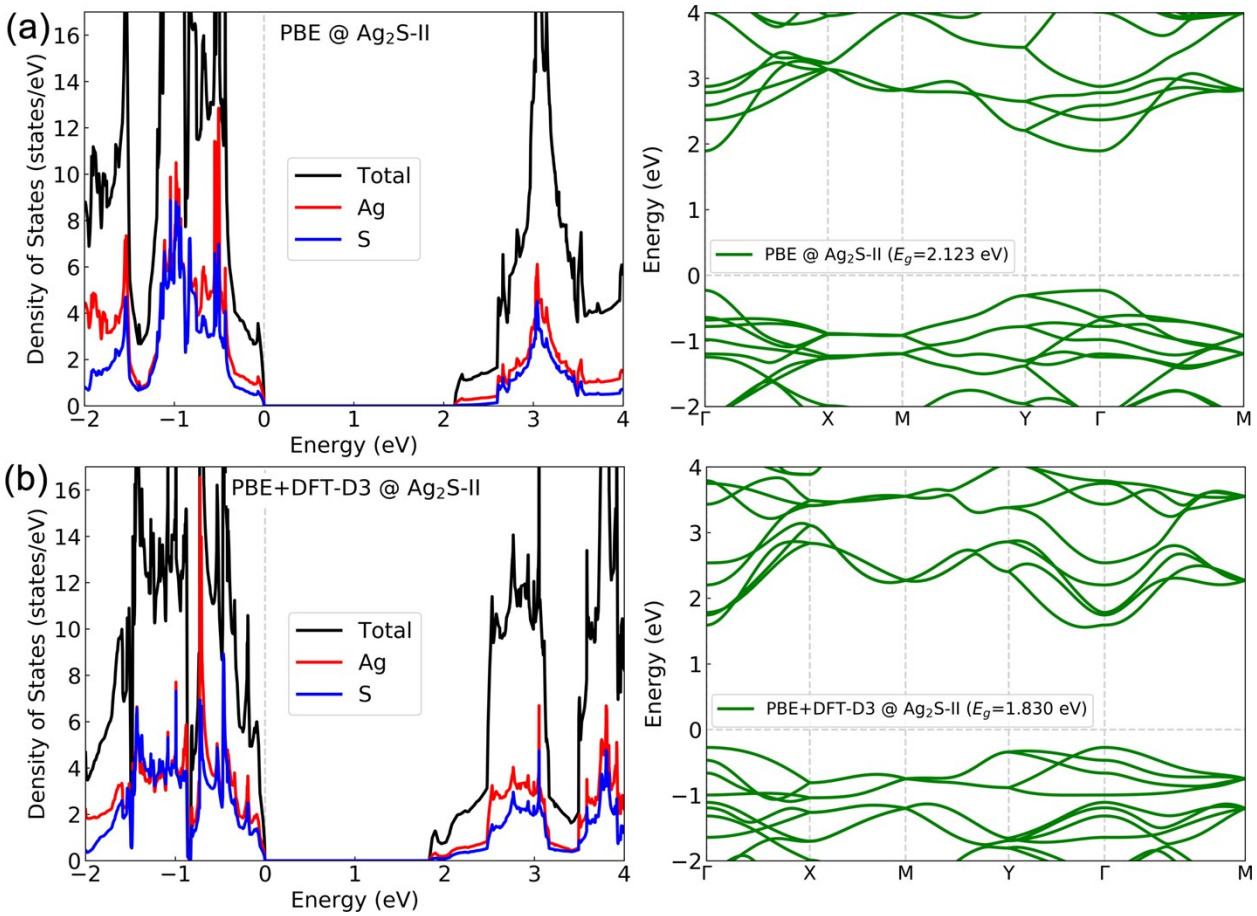

Figure S4. The density of states (DOS) (left panel) and the electronic band structure (right panel) of Ag_2S-II calculated using (a) the PBE functional and (b) the PBE functional with the DFT-D3 correction.

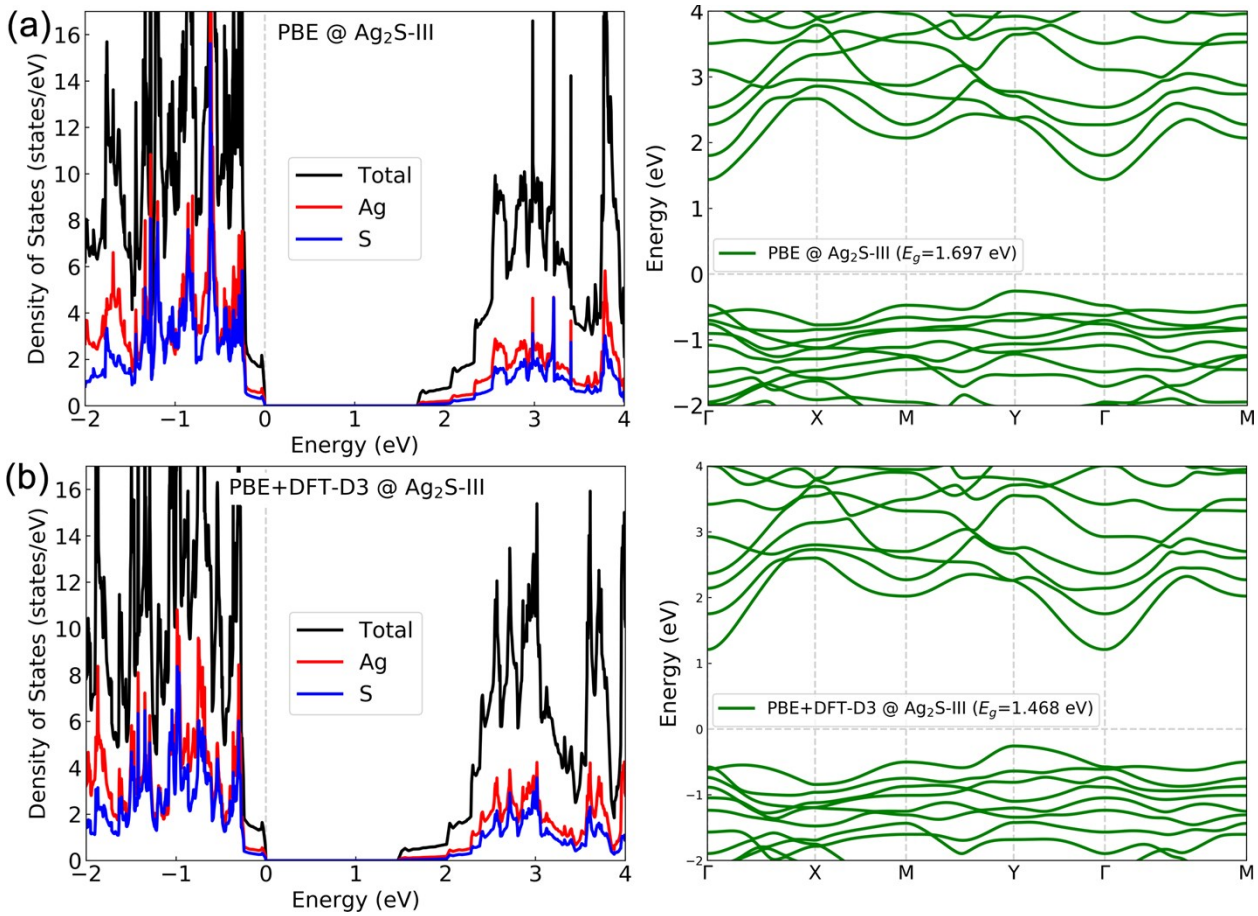

Figure S5. The density of states (DOS) (left panel) and the electronic band structure (right panel) of Ag_2S-III calculated using (a) the PBE functional and (b) the PBE functional with the DFT-D3 correction.

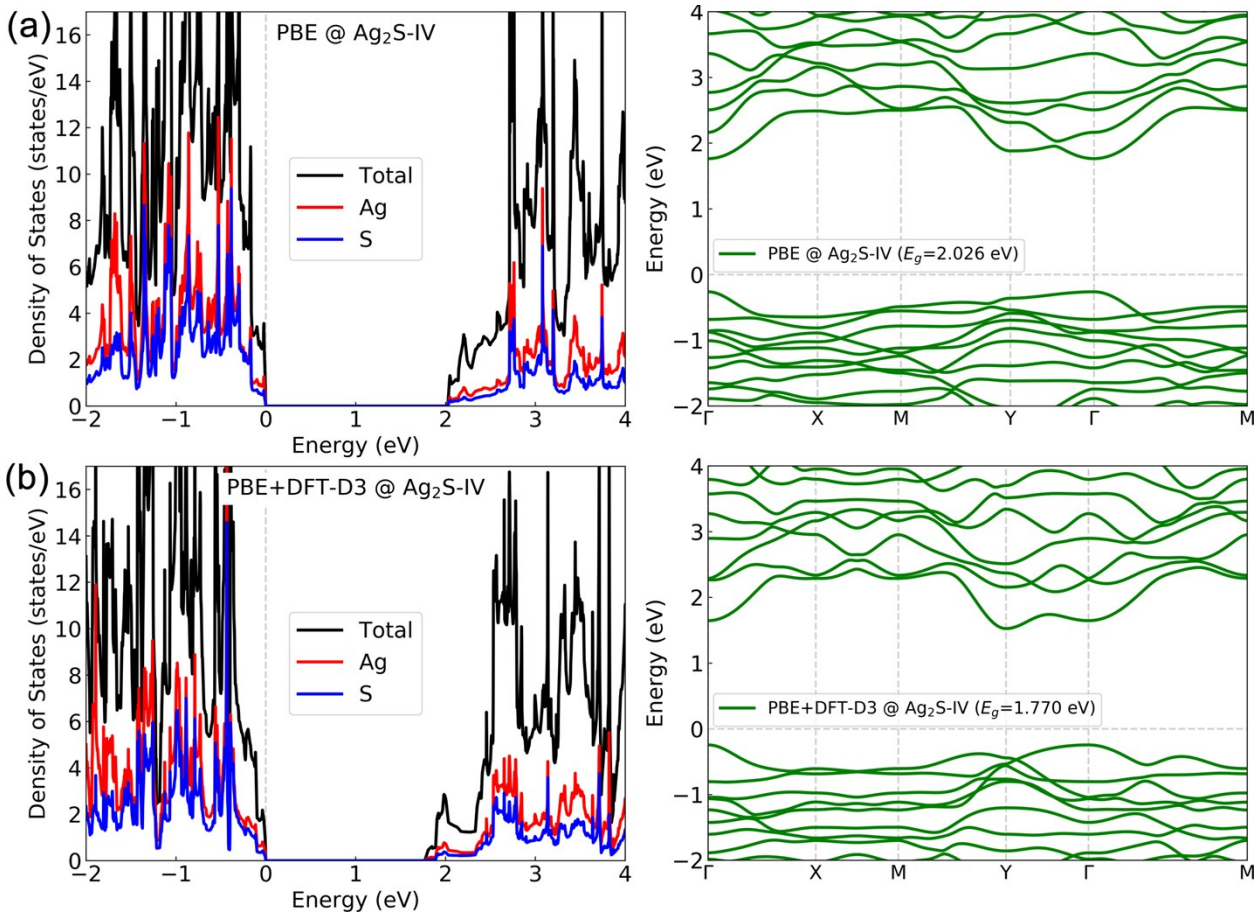

Figure S6. The density of states (DOS) (left panel) and the electronic band structure (right panel) of Ag_2S-IV calculated using (a) the PBE functional and (b) the PBE functional with the DFT-D3 correction.

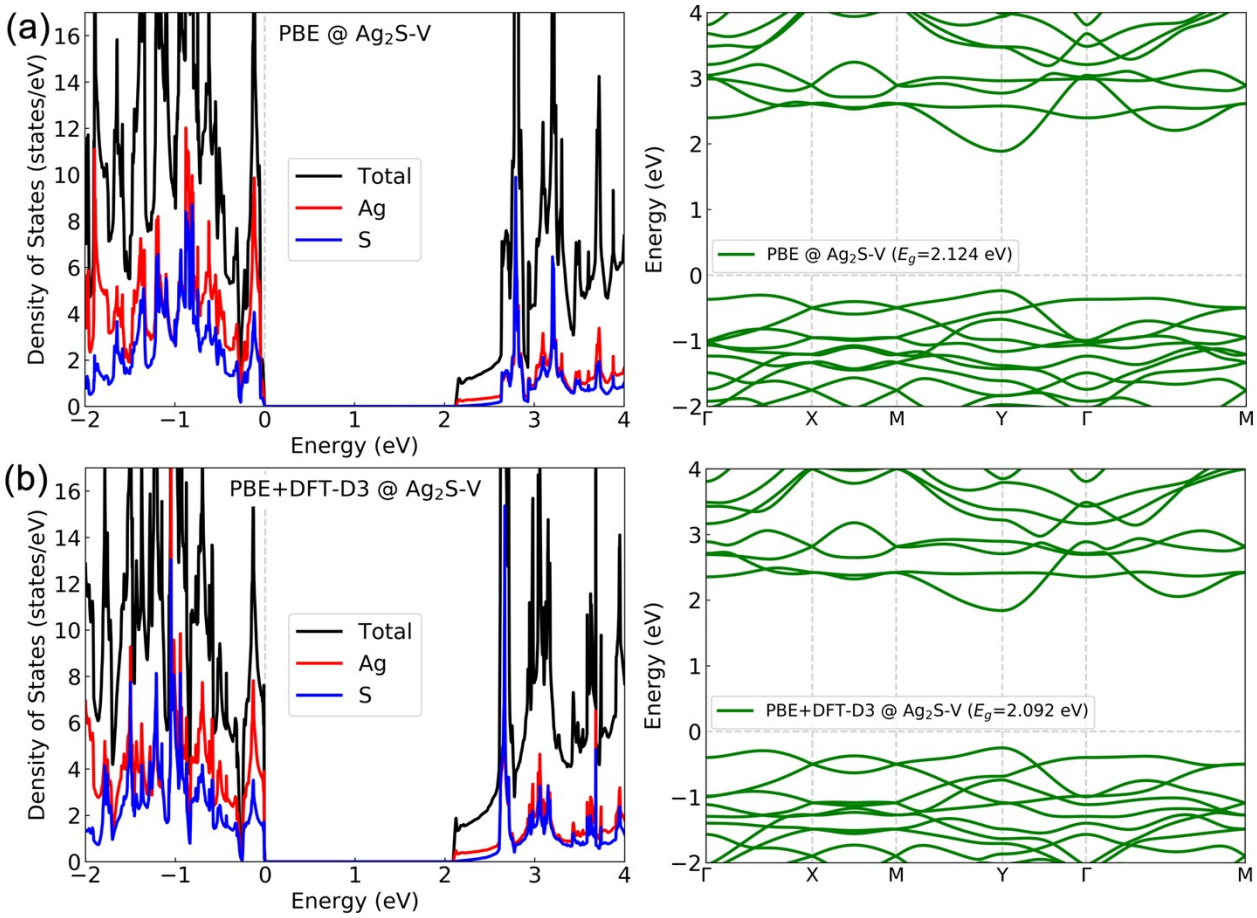

Figure S7. The density of states (DOS) (left panel) and the electronic band structure (right panel) of Ag_2S-V calculated using (a) the PBE functional and (b) the PBE functional with the DFT-D3 correction.

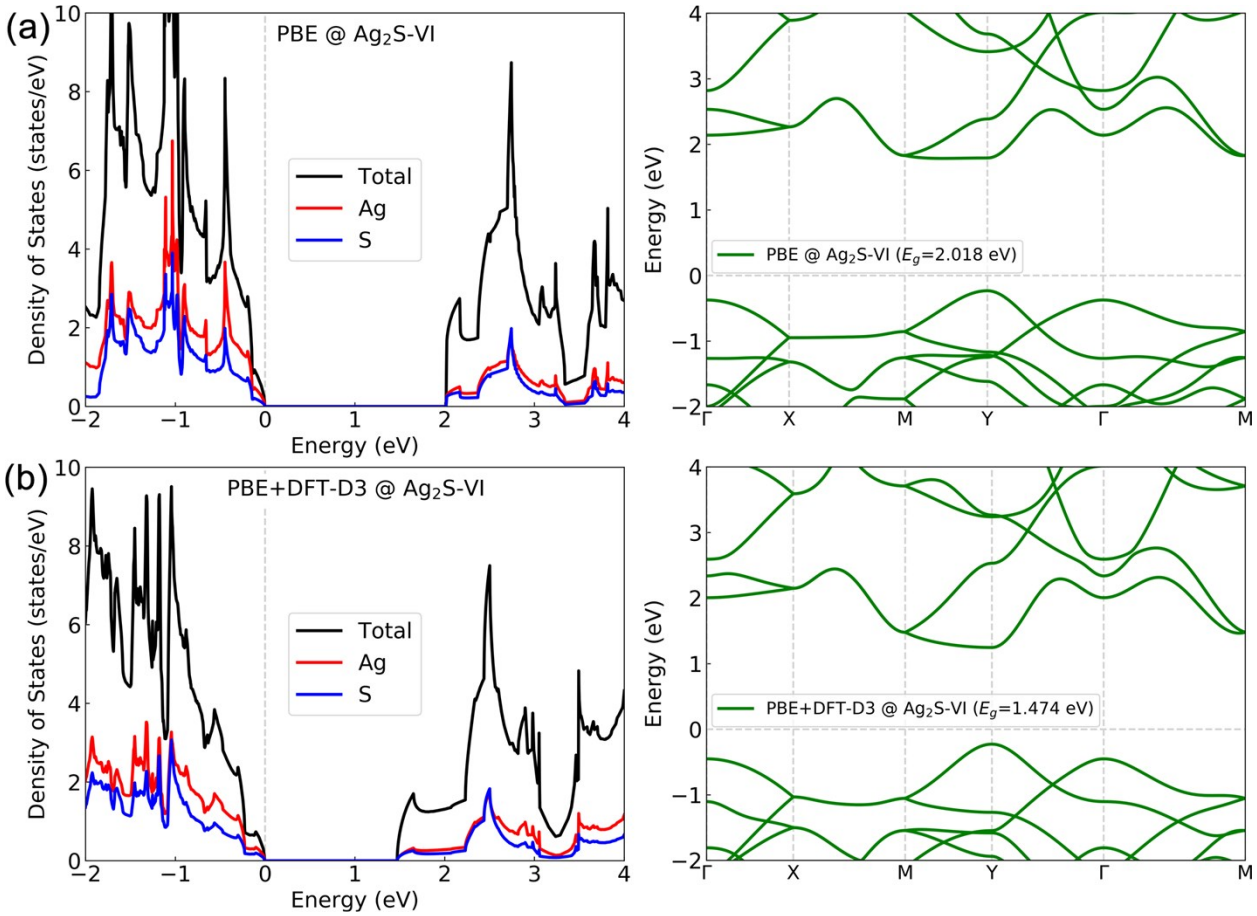

Figure S8. The density of states (DOS) (left panel) and the electronic band structure (right panel) of Ag_2S-VI (α-phase Ag_2S) calculated using (a) the PBE functional and (b) the PBE functional with the DFT-D3 correction.

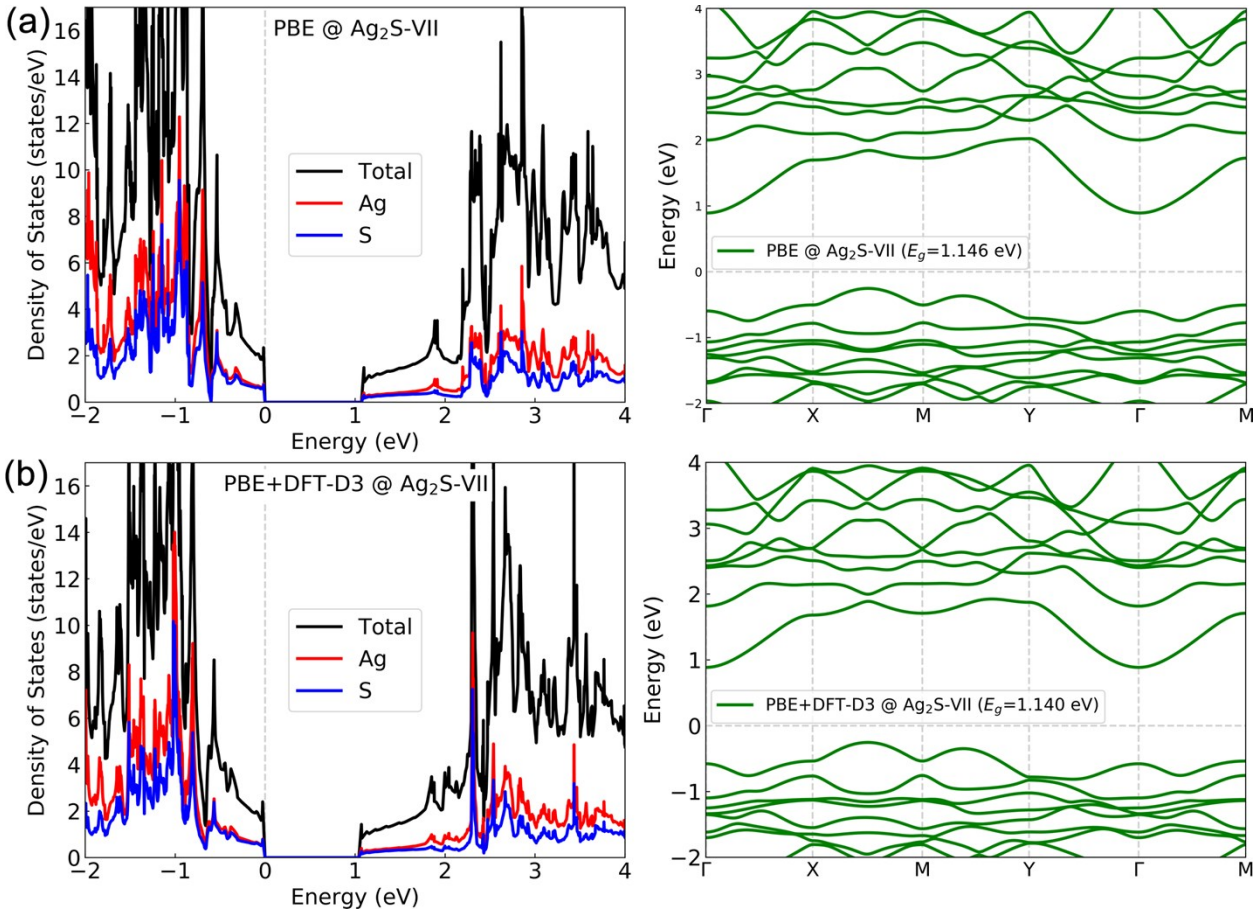

Figure S9. The density of states (DOS) (left panel) and the electronic band structure (right panel) of Ag_2S-VII calculated using (a) the PBE functional and (b) the PBE functional with the DFT-D3 correction.

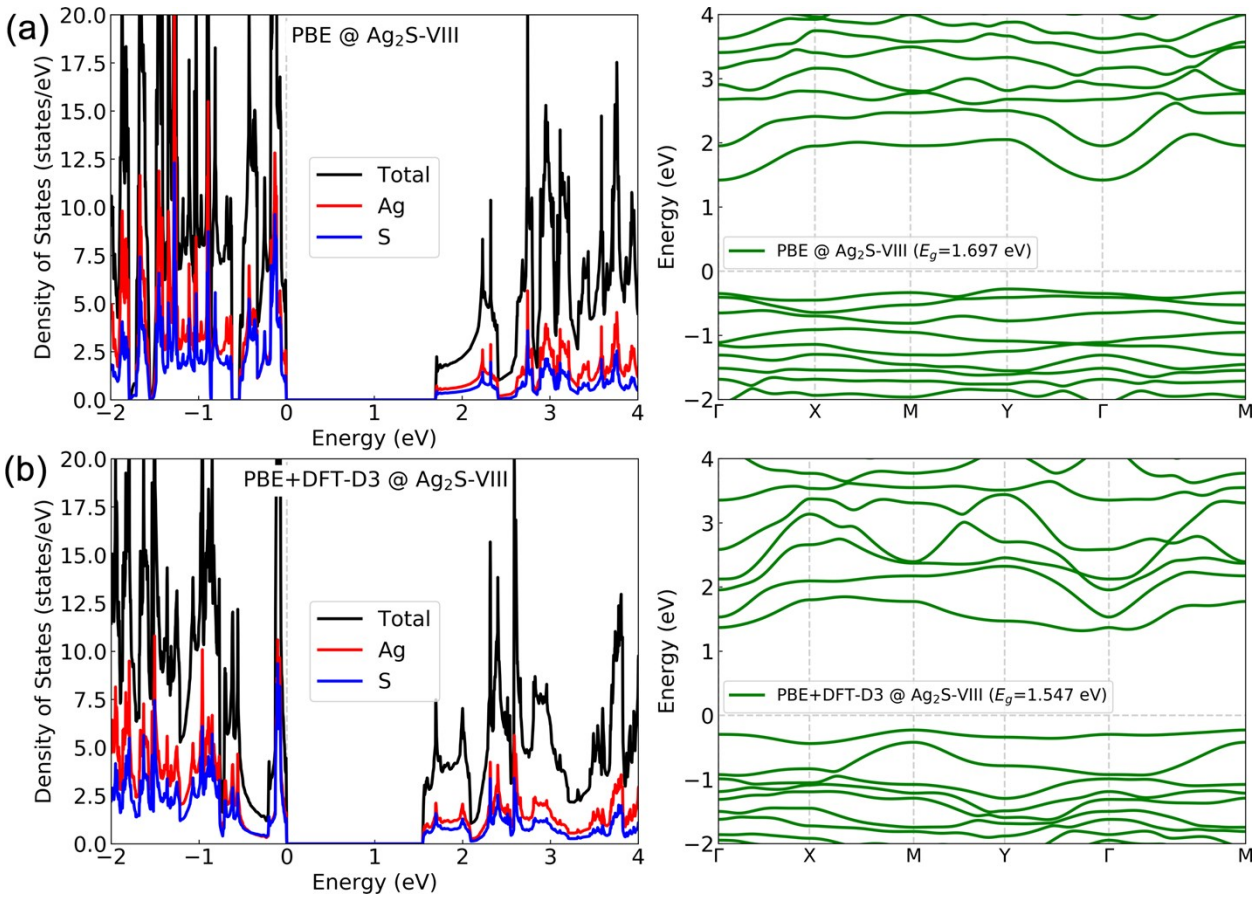

Figure S10. The density of states (DOS) (left panel) and the electronic band structure (right panel) of Ag_2S-VIII calculated using (a) the PBE functional and (b) the PBE functional with the DFT-D3 correction.

The phonon dispersion of the Lieb-lattice Ag_2S

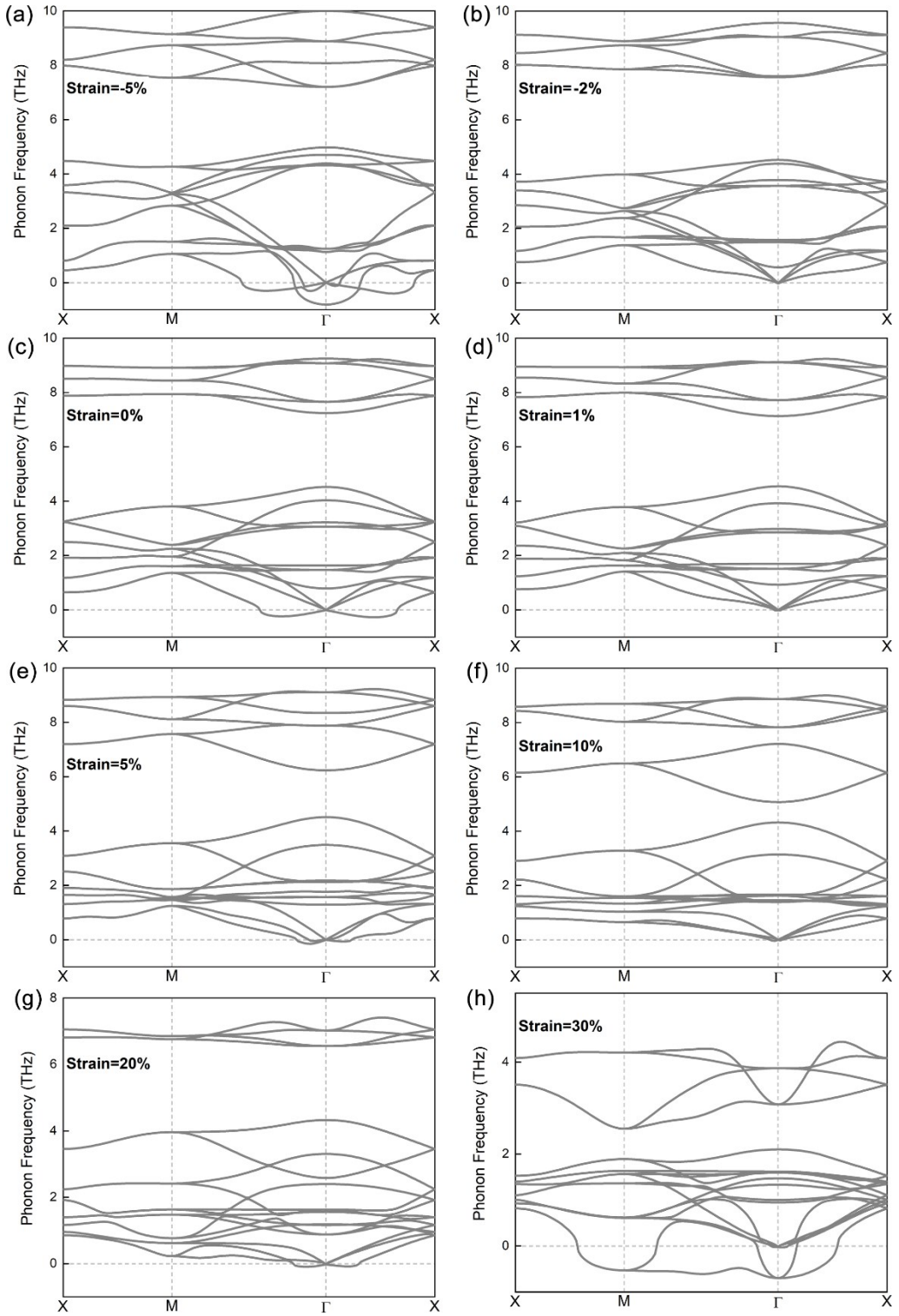

Figure S11. The phonon dispersion of the Lieb-lattice Ag_2S under a biaxial strain of (a) -5%, (b) -2%, (c) 0%, (d) 1%, (e) 5%, (f) 10%, (g) 20% and (h) 30%.

The phonon spectra of the strain-free and strained Lieb-lattice Ag_2S have been calculated. As shown in **Figure S11c**, there are minor imaginary vibrational frequencies around the Brillouin zone center, but they can be supressed by applying slight strains, *i.e.* -2% (**Figure S11b**) or 1% (**Figure S11d**). This indicates that Ag_2S can be dynamically stabilized by slight strains which can be realized by an appropriate substrate. As shown in **Figure S11a**, however, a compressive strain of -5% leads to plenty of imaginary phonon modes, indicative of the dynamical instability of Ag_2S in this case. On the other hand, when Ag_2S is stretched by 5%, 10% or 20%, there is lack of imaginary vibrational frequencies or they are only minor, indicating that stretched Ag_2S is likely to be dynamically stable or can be stabilized by substrates. At the strain of 30%, however, the phonon calculation suggests the dynamical instability of the strained Ag_2S (**Figure S11h**).

The *ab initio* molecular dynamics simulations of the Lieb-lattice Ag_2S

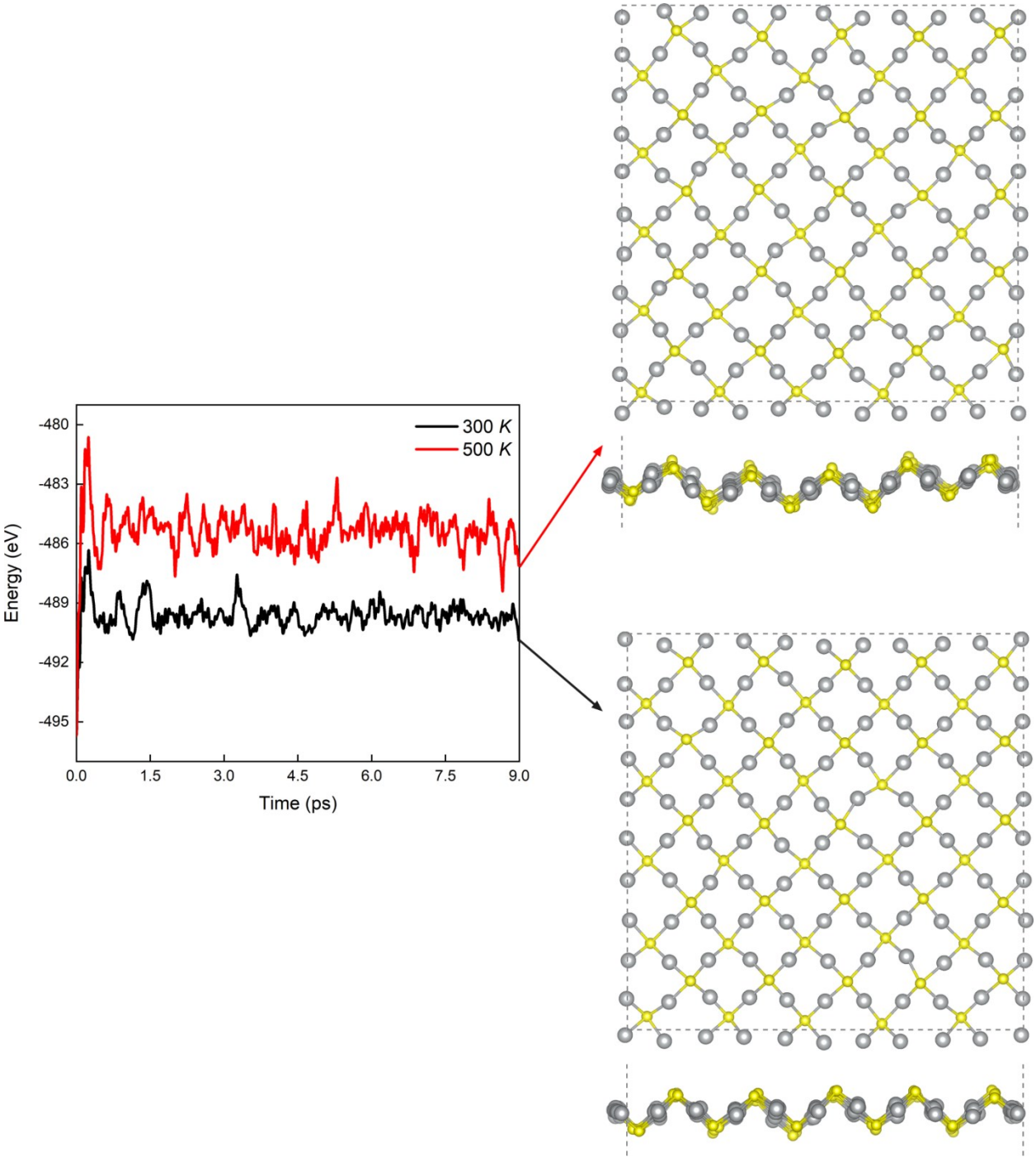

Figure S12. The energy evolution of the 5×5 supercell during a 9-ps *ab initio* molecular dynamics (AIMD) simulation at 300 K (black) and 500 K (red). The top and side view of the atomic structure of the Lieb-lattice Ag_2S after the AIMD simulation at 300 K and 500 K are shown in the right panel.

The chemical stability of Lieb-lattice Ag_2S

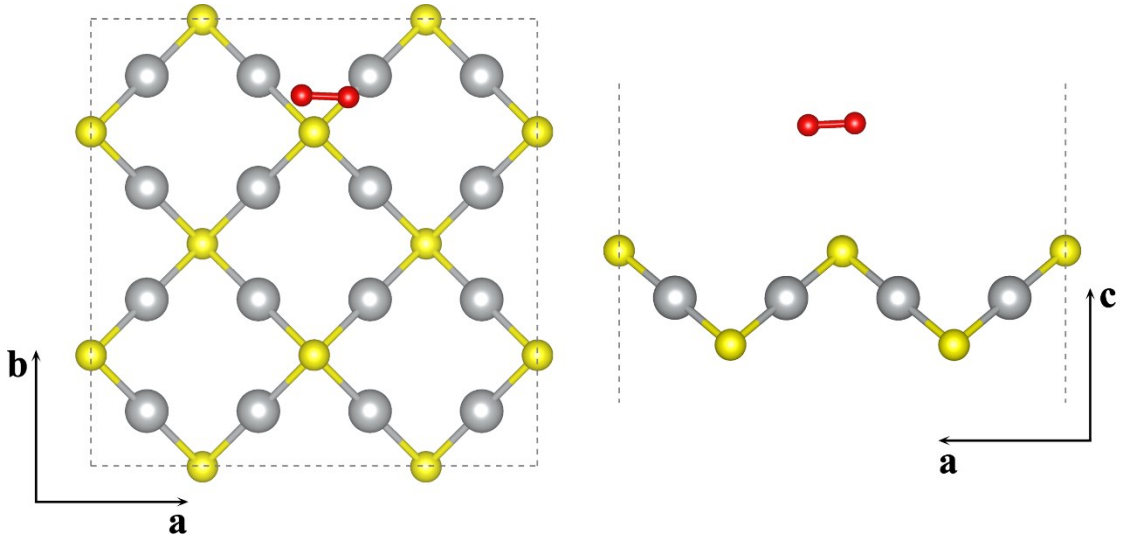

Figure S13. The top (left panel) and side (right panel) view of oxygen adsorption on the 2×2 Lieb-lattice Ag_2S supercell. The oxygen molecule (O_2) is 3.546 Å apart from Lieb-lattice Ag_2S, indicating that the adsorption is in the weak physisorption range and hence Ag_2S is likely to be stable under the oxygen atmosphere.

The electronic structure of the Lieb-lattice Ag_2S at the HSE06 level

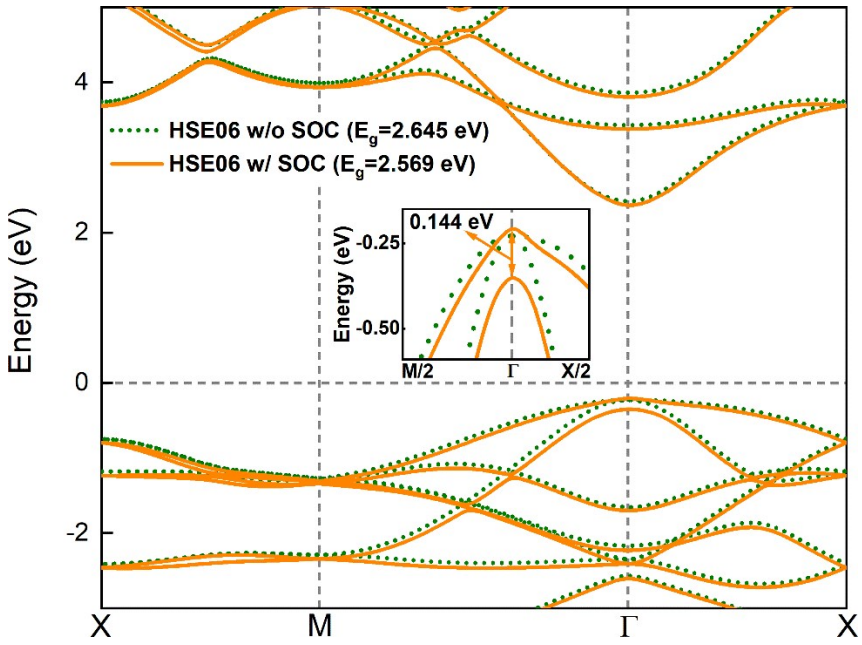

Figure S14. The band structure of the Lieb-lattice Ag_2S at the HSE06 level without and with the spin-orbit coupling (SOC) included. Inset: the zoom-in band dispersion around the valance band maximum (VBM) at the Γ point.

Band projections and spin projections of the electronic structure of the Lieb-lattice Ag_2S at the PBE level

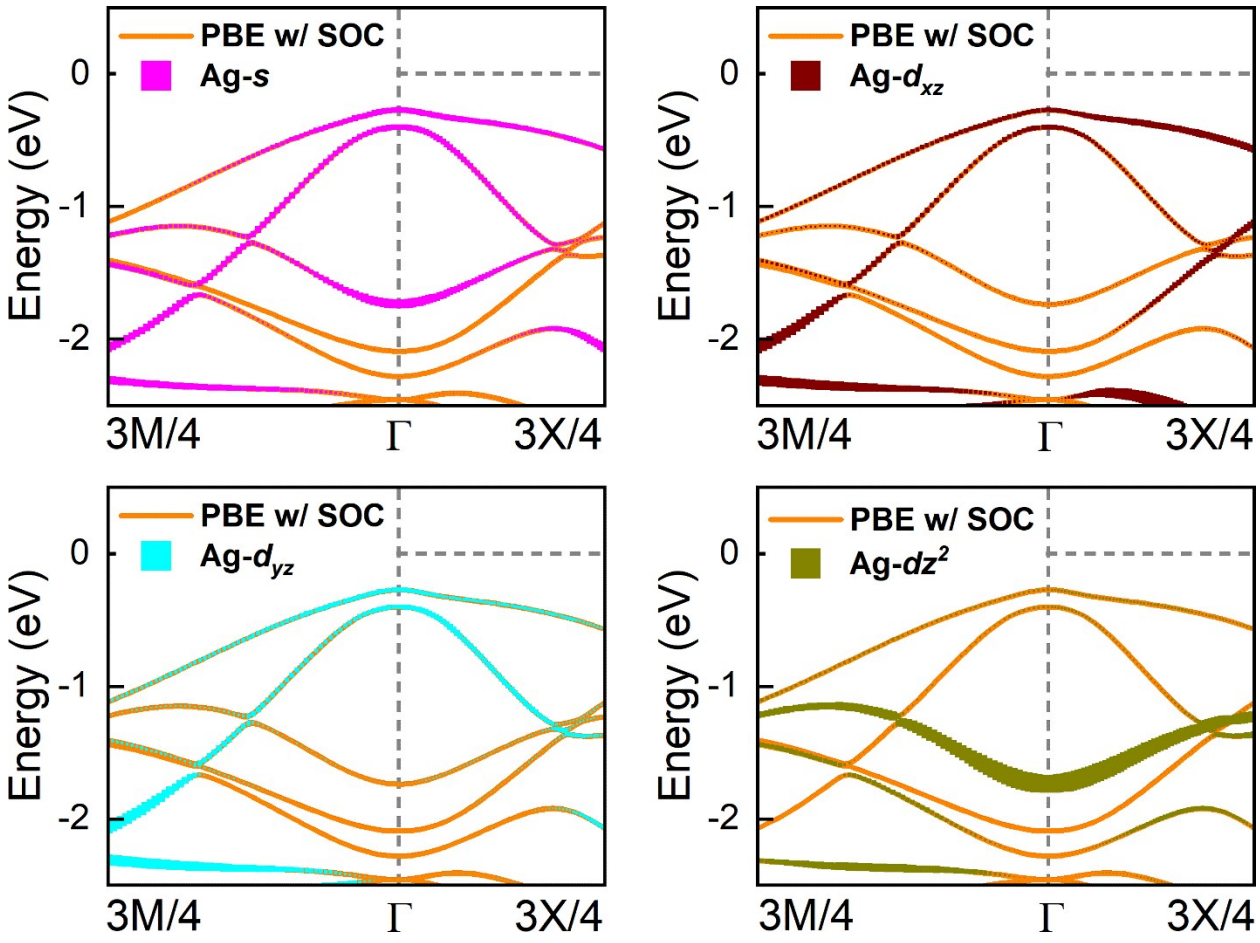

Figure S15. The projection of the electronic states on the Ag-*s*, Ag-d_{xz}, Ag-d_{yz} and Ag-d_{z^2} orbital, respectively. The calculation is at the PBE level with the spin-orbit coupling (SOC) included. It is noted that the subscript of the *k*-point of $\sqrt{2}$ is omitted.

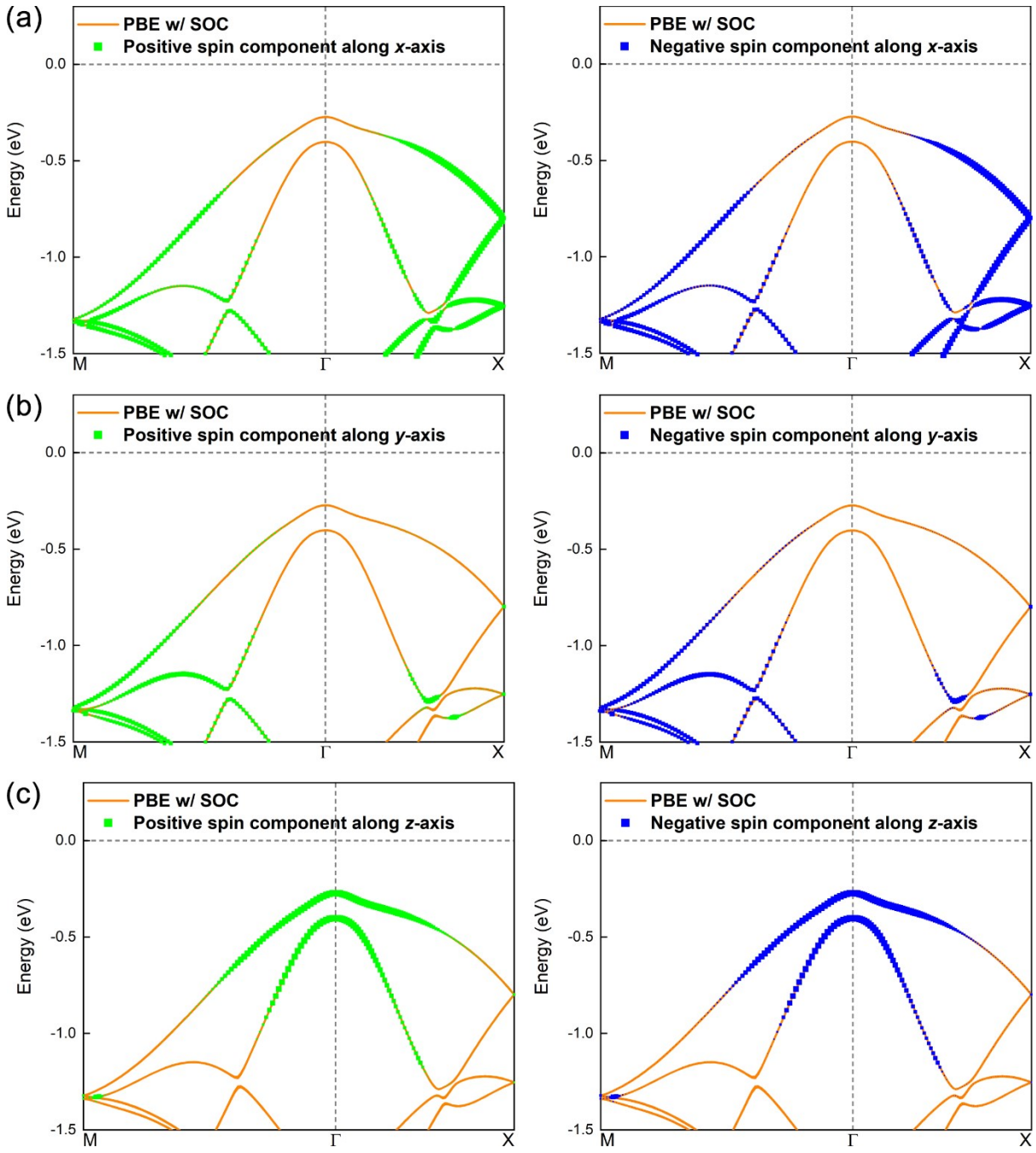

Figure S16. The spin projection of the electronic band structure of Lieb-lattice Ag_2S along (a) the x-axis, (b) the y-axis and (c) the z-axis. Left (right) panel: the positive (negative) spin component. The band structure is at the PBE level with the spin-orbit coupling (SOC) included.

The Rashba-type spin-orbital coupling (SOC) could be another term in the TB model, but it is usually very small compared with the intrinsic SOC in Eq. (2).[18] This also holds for Lieb-lattice Ag_2S, where the degeneracy at the Γ point is mainly lifted by the intrinsic SOC. The small Rashba-

type SOC in Lieb-lattice Ag_2S is indicated by the spin projection in **Figure S16**. One can see that the spin degeneracy remains.

The tight-binding model fitted to the PBE and HSE06 bands

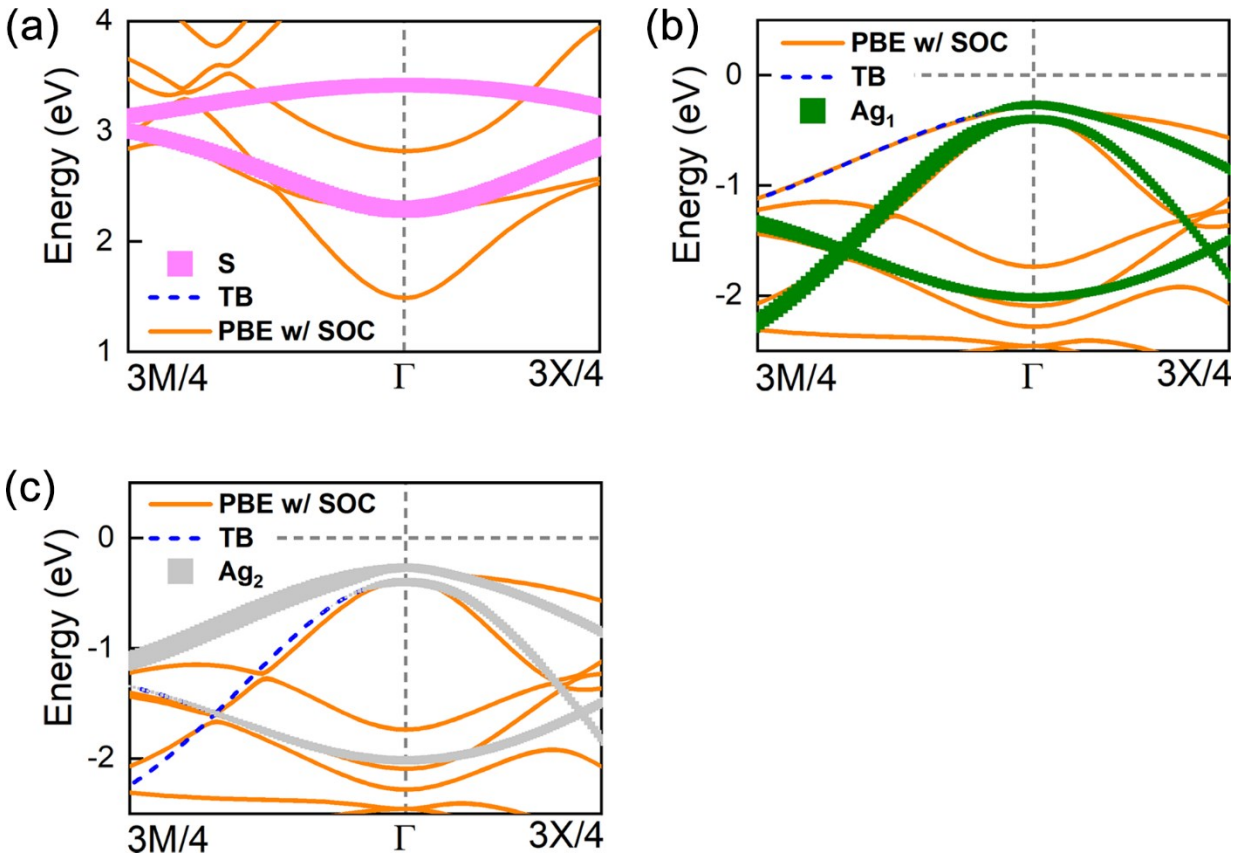

Figure S17. The projection of the TB bands fitted to the DFT bands onto (a) the S site, (b) the Ag_1 site and (c) the Ag_2 site, respectively. The DFT bands are calculated at the PBE level with the SOC. The fitted parameters are tabulated in **Table S2**. It is noted that the subscript of the *k*-point of $\sqrt{2}$ is omitted.

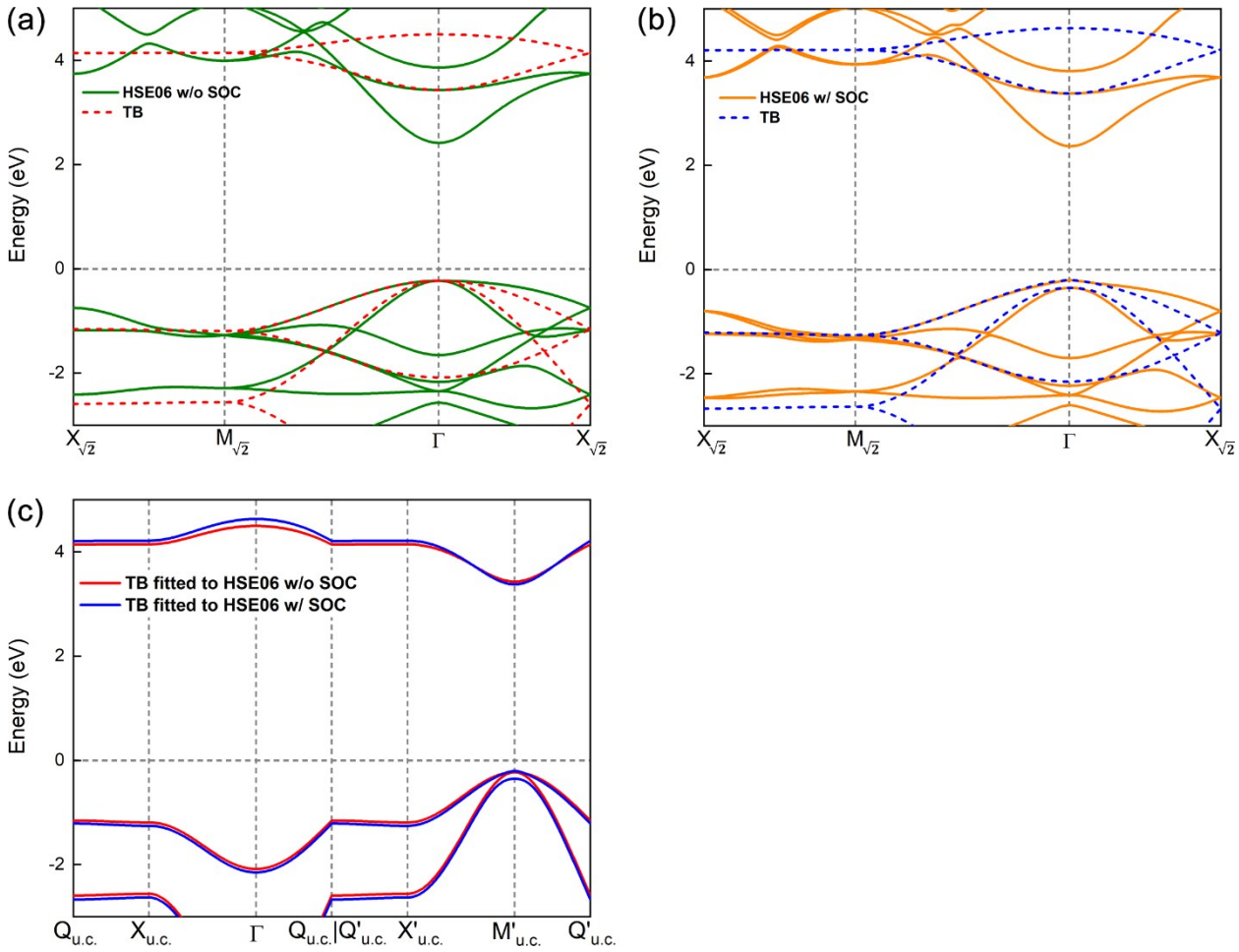

Figure S18. The tight-binding model of the Lieb-lattice Ag_2S fitted to the HSE06 band structure (a) without and (b) with the SOC. (c) The fitted TB bands are unfolded into the 1BZ of the planar Lieb lattice. The fitted parameters are tabulated in **Table S2**.

Selectively switch off neighboring interactions and the onsite energy difference in the TB model

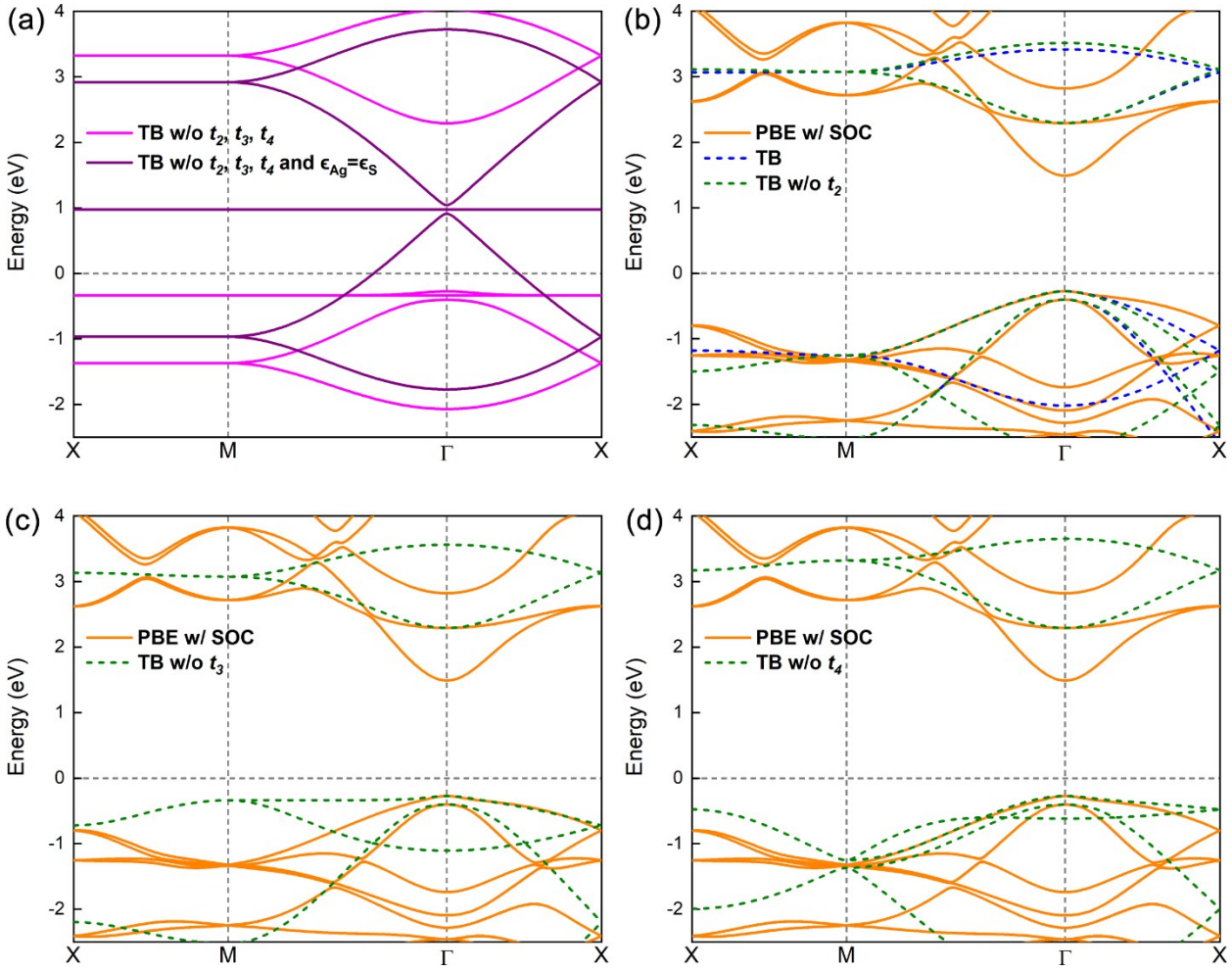

Figure S19. The tight-binding model of the Lieb-lattice Ag_2S fitted to the PBE band structure calculated with the SOC. The neighboring interactions and the difference in the onsite energy between the Ag site and S site are selectively switched off in the fitted TB model. The fitted parameters are tabulated in **Table S2**. It is noted that the subscript of the *k*-point of $\sqrt{2}$ is omitted.

The biaxial strain effect on the Ag-S bond stability of Lieb-lattice Ag_2S

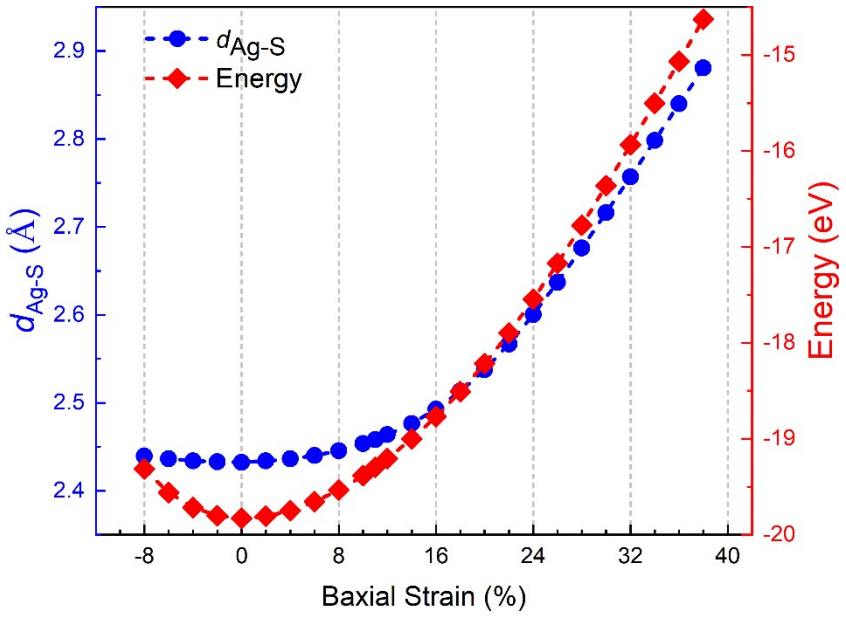

Figure S20. The Ag-S bond length (d_{Ag-S}) (solid circle) and the total energy (solid diamond) of Lieb-lattice Ag_2S as functions of the biaxial in-plane strain.

Figure S20 shows that the Ag-S bond length continuously increases when a biaxial strain of up to 38% is applied. At the biaxial strain of 38%, the Ag-S bond length (2.881 Å) is within the upper bond limit proposed by Mounet et al. *i.e.* $r_{Ag}^{vdW} + r_{S}^{vdW} - 1.5 = 2.92$ Å, where r_{i}^{vdW} is the van der Waals (vdW) radius of atomic species i.[19, 20] This indicates that the Ag-S bond still remains, which is also suggested by the steady and gradual increase in the calculated total energy of strained Lieb-lattice Ag_2S (**Figure S20**).

The Poisson ratio of the Lieb-lattice Ag_2S

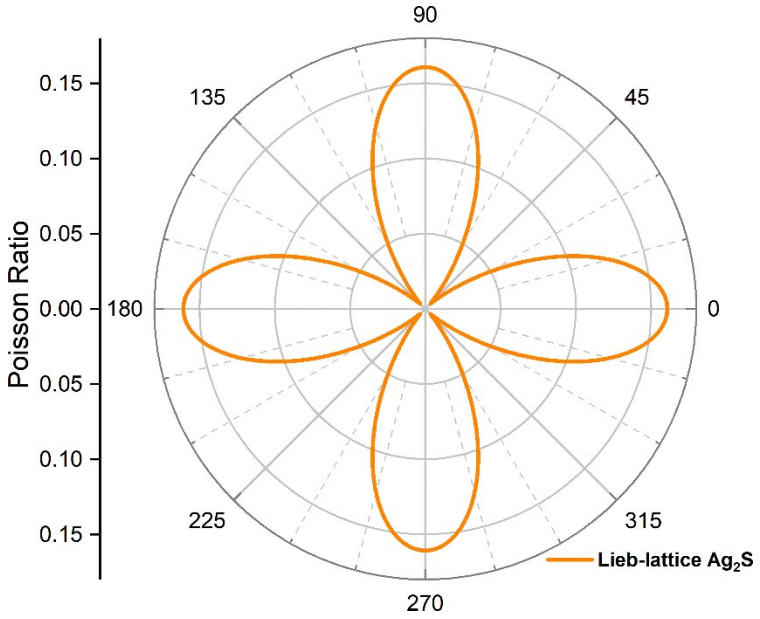

Figure S21. The Poisson ratio of the Lieb-lattice Ag_2S.

The Poisson ratio ($v_{\vec{n}}$) along an arbitrary in-plane direction $\vec{n} = \cos(\theta)\vec{e}_x + \sin(\theta)\vec{e}_y$ can be estimated as follows[21]

$$v_{\vec{n}} = \frac{\left(C_{11} + C_{22} - \frac{\Delta}{C_{44}}\right)c^2s^2 - C_{12}(c^4 + s^4)}{C_{11}s^4 + C_{22}c^4 + \left(\frac{\Delta}{C_{44}} - 2C_{12}\right)c^2s^2} \quad (S10)$$

where $\Delta = C_{11}C_{12} - C_{12}^2$, $c = \cos(\theta)$ and $s = \sin(\theta)$. $C_{11} = C_{22}$, C_{12} and C_{44} are the calculated elastic constants. As shown in **Figure S21**, the Poisson ratio of Lieb-lattice Ag_2S reaches its maximum along the *x*- and *y*-direction, whereas along the diagonal direction the ratio reaches its minimum and approaches zero. It should be noted that the Poisson ratio of Lieb-lattice Ag_2S monolayer is always positive – the absence of negative Poisson ratio, in agreement with the recent report.[22]

In addition to the calculation approach discussed above, Ref. [22] also explicitly computed the Poisson ratio along the diagonal direction according to the definition, $v = -d\varepsilon_\beta/d\varepsilon_\alpha$, where ε_α and ε_β indicate the relative strain along α- and β-direction, respectively. In this way, the Poisson ratio

of Lieb-lattice Ag_2S monolayer estimates to be negative along the diagonal direction, ranging from -0.2 to 0.[22] Noting that the linear elasticity approximation is adopted in the first approach, we believe that the second approach is more accurate. Therefore, Lieb-lattice Ag_2S is likely to exhibit a negative Poisson ratio along the diagonal direction.

The biaxial strain effect on the electronic structure of the Lieb-lattice Ag_2S

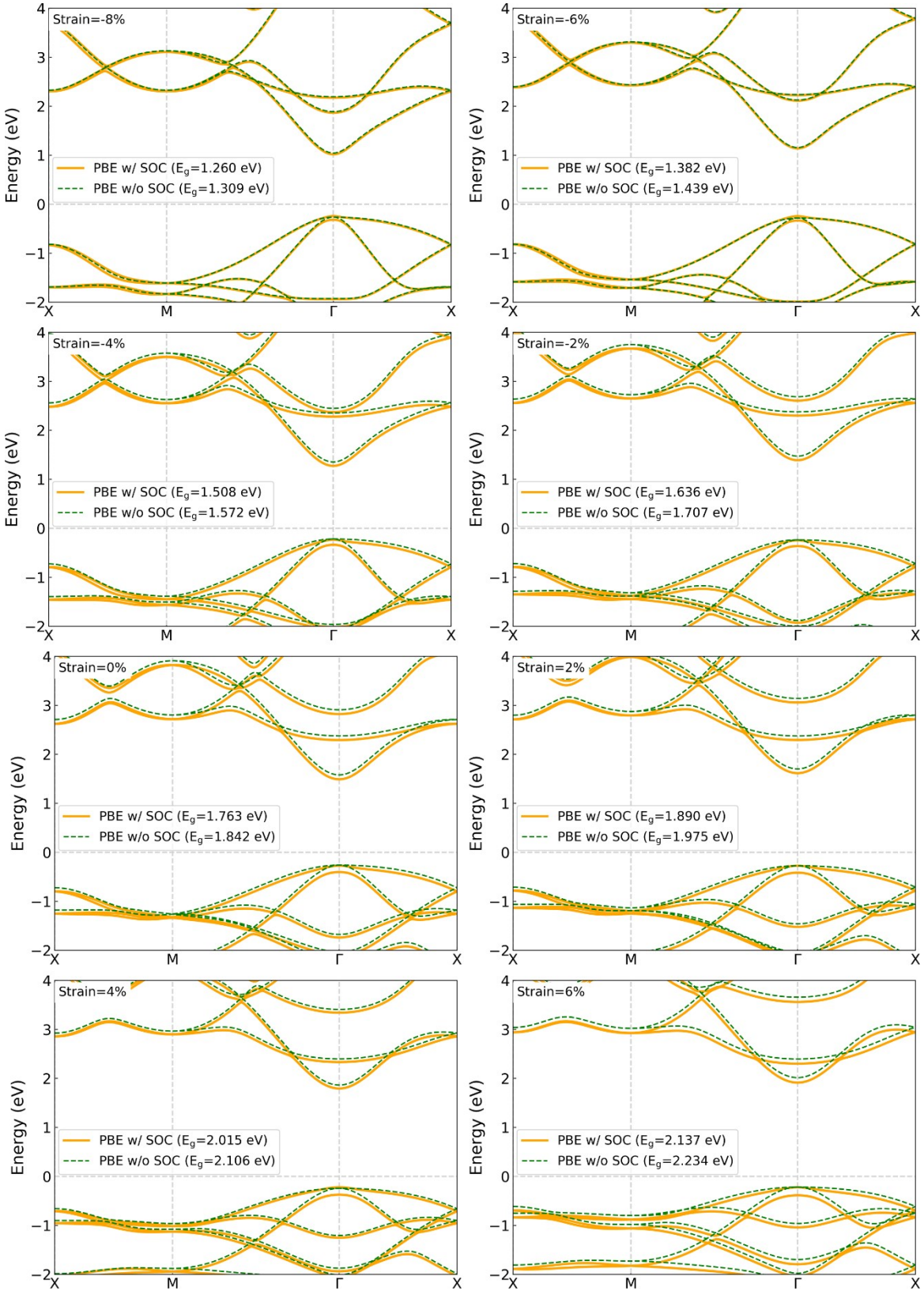

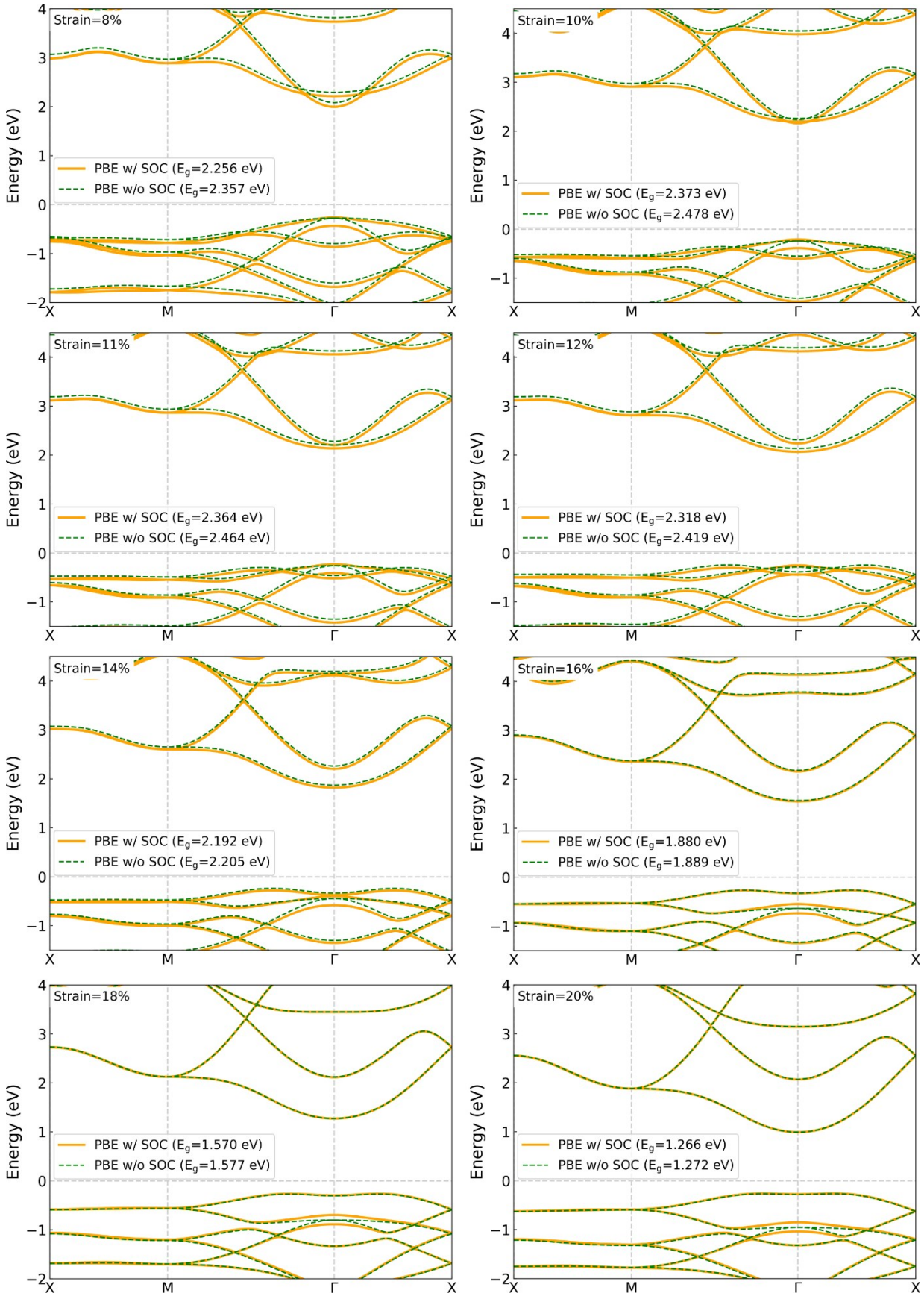
Strain=8%
PBE w/ SOC (Eg=2.256 eV)
PBE w/o SOC (Eg=2.357 eV)
Strain=10%
PBE w/ SOC (Eg=2.373 eV)
PBE w/o SOC (Eg=2.478 eV)
Strain=11%
PBE w/ SOC (Eg=2.364 eV)
PBE w/o SOC (Eg=2.464 eV)
Strain=12%
PBE w/ SOC (Eg=2.318 eV)
PBE w/o SOC (Eg=2.419 eV)
Strain=14%
PBE w/ SOC (Eg=2.192 eV)
PBE w/o SOC (Eg=2.205 eV)
Strain=16%
PBE w/ SOC (Eg=1.880 eV)
PBE w/o SOC (Eg=1.889 eV)
Strain=18%
PBE w/ SOC (Eg=1.570 eV)
PBE w/o SOC (Eg=1.577 eV)
Strain=20%
PBE w/ SOC (Eg=1.266 eV)
PBE w/o SOC (Eg=1.272 eV)
Energy (eV)
X
M
Γ
X

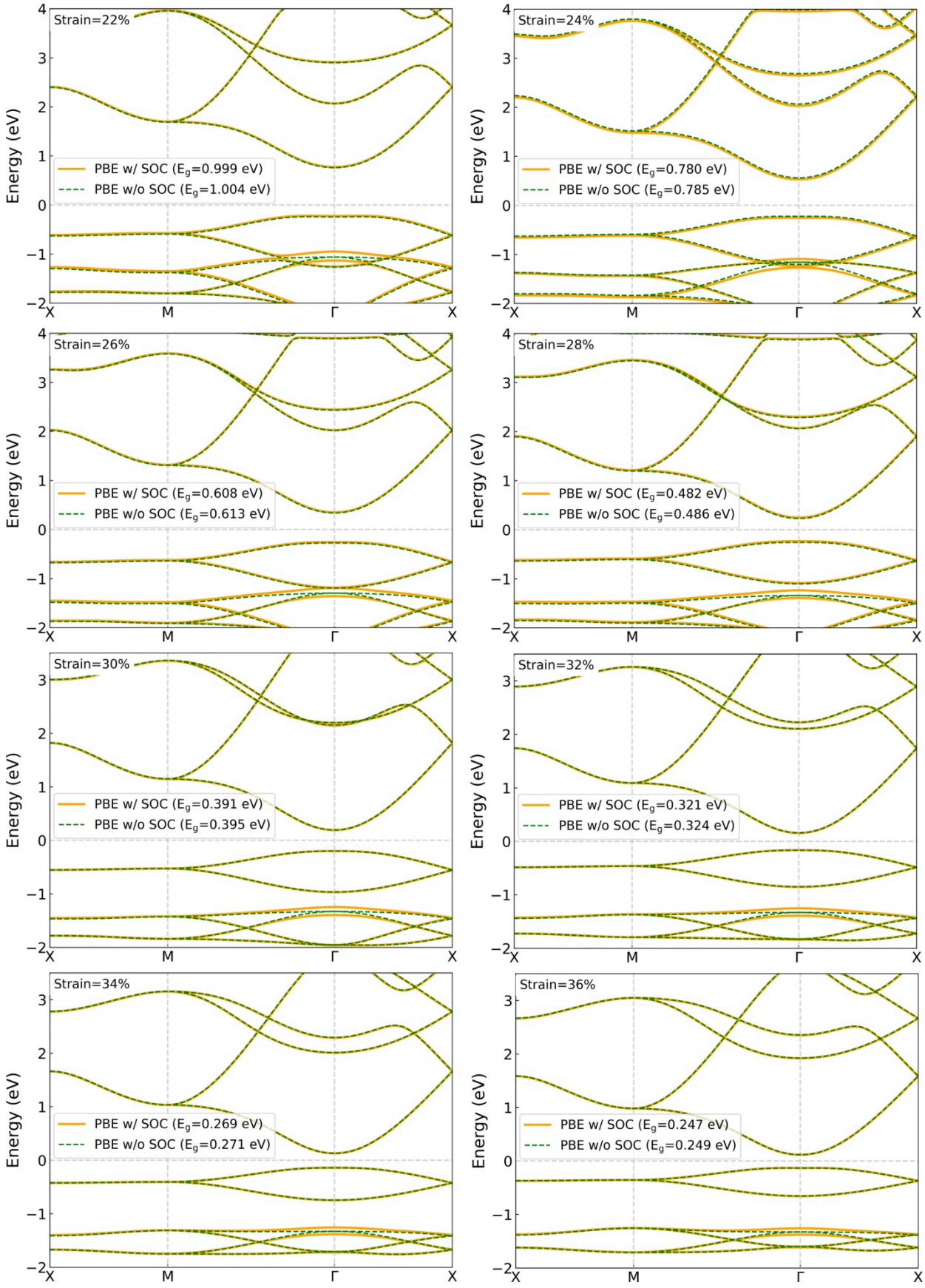
Strain=22%
PBE w/ SOC (Eg=0.999 eV)
PBE w/o SOC (Eg=1.004 eV)
Strain=24%
PBE w/ SOC (Eg=0.780 eV)
PBE w/o SOC (Eg=0.785 eV)
Strain=26%
PBE w/ SOC (Eg=0.608 eV)
PBE w/o SOC (Eg=0.613 eV)
Strain=28%
PBE w/ SOC (Eg=0.482 eV)
PBE w/o SOC (Eg=0.486 eV)
Strain=30%
PBE w/ SOC (Eg=0.391 eV)
PBE w/o SOC (Eg=0.395 eV)
Strain=32%
PBE w/ SOC (Eg=0.321 eV)
PBE w/o SOC (Eg=0.324 eV)
Strain=34%
PBE w/ SOC (Eg=0.269 eV)
PBE w/o SOC (Eg=0.271 eV)
Strain=36%
PBE w/ SOC (Eg=0.247 eV)
PBE w/o SOC (Eg=0.249 eV)
Energy (eV)
X
M
Γ
X

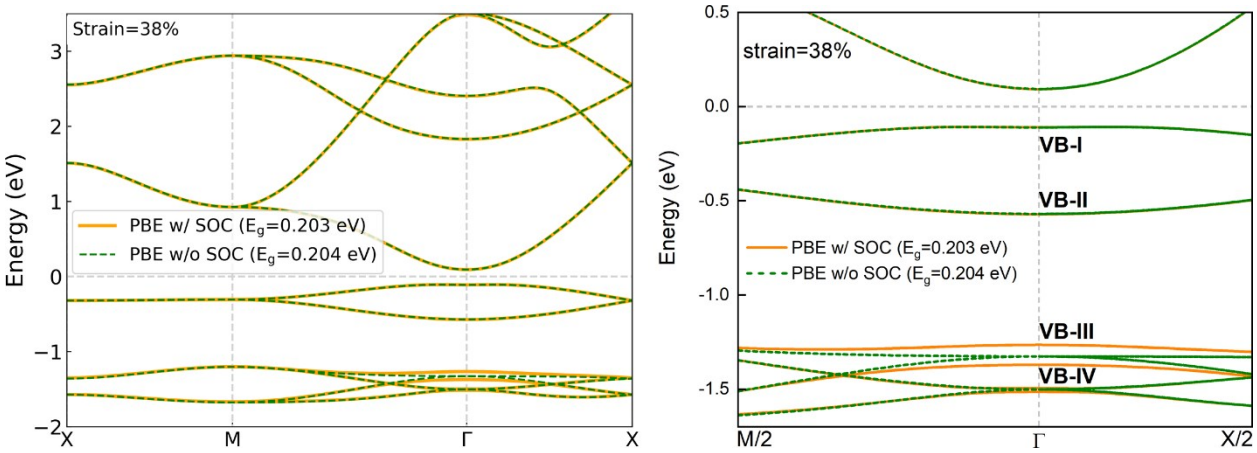

Figure S22. The electronic band structure of the Lieb-lattice Ag_2S as a function of the biaxial strain ranging from -8% to 38%. The calculations are at the PBE level without (green dashed line) and with (orange solid line) the SOC interaction included. The last panel is the zoom-in view of the electronic band structure of the 38% strained Ag_2S. It is noted that the subscript of the *k*-point of $\sqrt{2}$ is omitted.

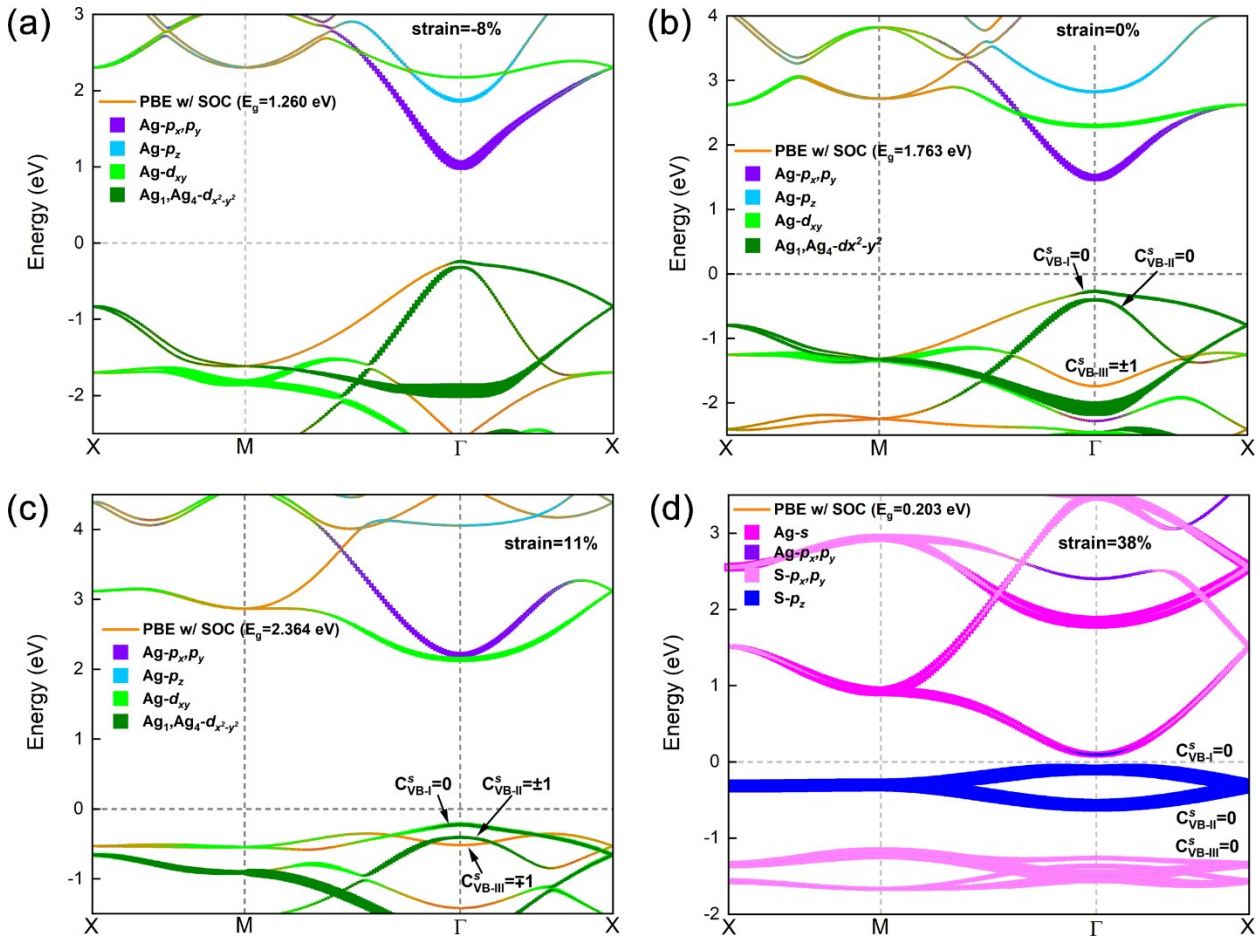

Figure S23. The electronic band structure of the Lieb-lattice Ag_2S at the PBE level with SOC under the biaxial strain of (a) -8%, (b) 0%, (c) 11% and (d) 38%, respectively. In panels (a-c), selective projections on the Ag orbitals are shown to clarify the band evolution and switching. In panel (d), the Ag and S orbitals which are not present in the panel contribute little to the electronic states around CBM and VBM. The calculated spin Chern numbers of the three highest valence bands are marked in panels (b-d).

As shown in **Figure S23**, since the spin Chern number is always zero for VB-I, Lieb-lattice Ag_2S is a topologically trivial semiconductor regardless of tensile strains which have been studied in the present work. But for VB-II and VB-III, they have nonzero spin Chern number at the strain of 11%. We noticed that spin Chern number is usually not well-defined in the presence of SOC, but numerically, we can always get these values. Although we must say there is no real physical reason to calculate Z_2 for specific bands here, as a cross check, we calculated Z_2 which equals 1 by counting the parities of VB-II / VB-III at all time-reversal momentum. This result also agrees well with the physical relation between spin Chern number and Z_2 invariants.

It is noted that at the biaxial strain of 38%, the VB-I and VB-II (**Figure S23d**) do not correspond to the flat band and the lower Dirac band, respectively. In the case of the strain-free Ag_2S, these S-p_z dominated valence bands are deep valence bands, *i.e.* VB-III and VB-V in **Figure 2b**. They are pushed upwards in energy by the strain of 38% and become new VB-I and VB-II (**Figure S23d**). At the biaxial strain of 38%, VB-III and VB-IV (the last panel of **Figure S22**) are instead identified as the flat band and the lower Dirac band, respectively, as suggested by the SOC-induced degeneracy lifting at the Γ point.

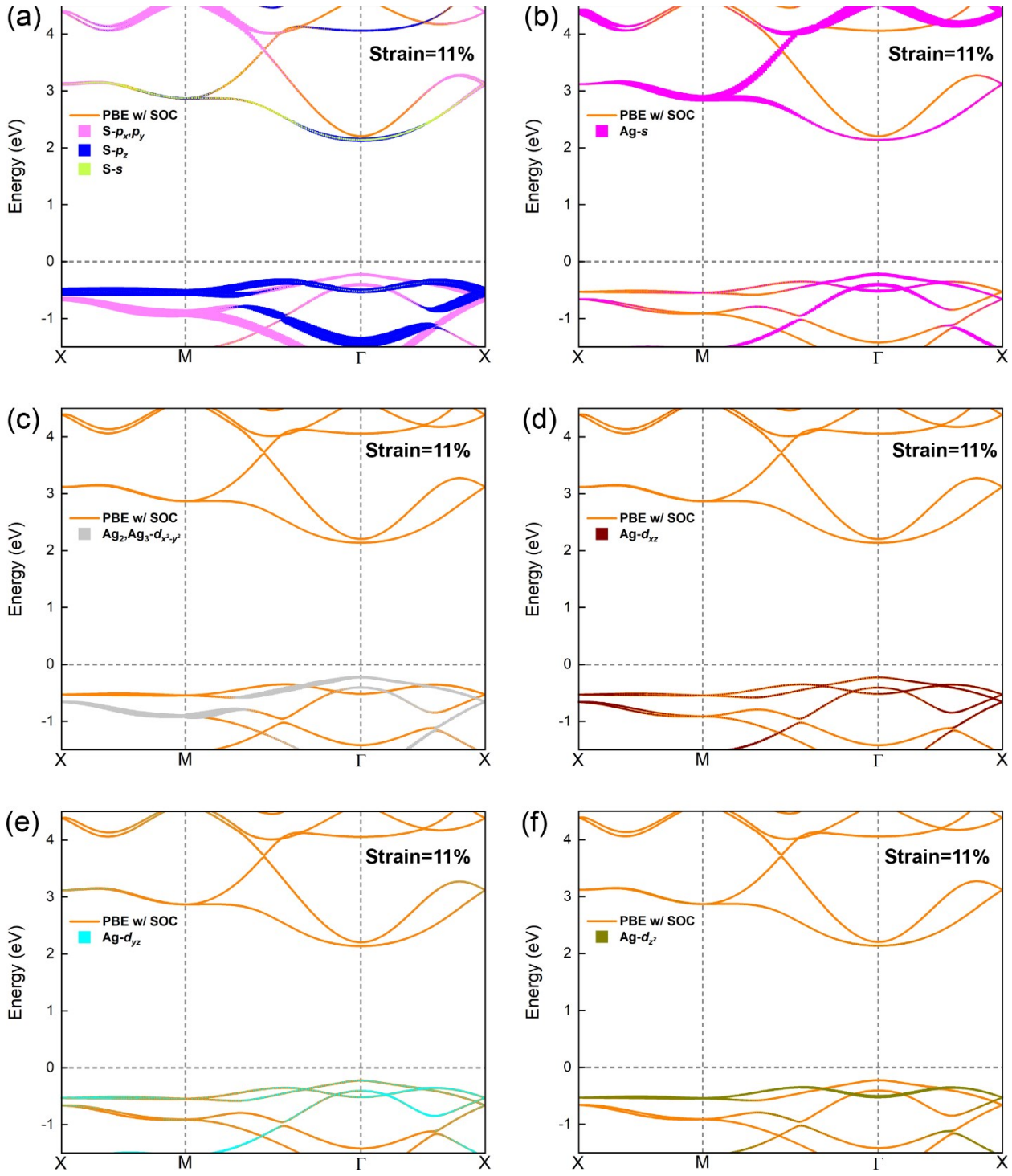

Figure S24. The projected band structure of the Lieb-lattice Ag_2S under a biaxial strain of 11%. The projection onto other Ag orbitals under the strain of 11% is shown in **Figure 5b**.

The band switch between CB-I and CB-II at the biaxial strain of 11%

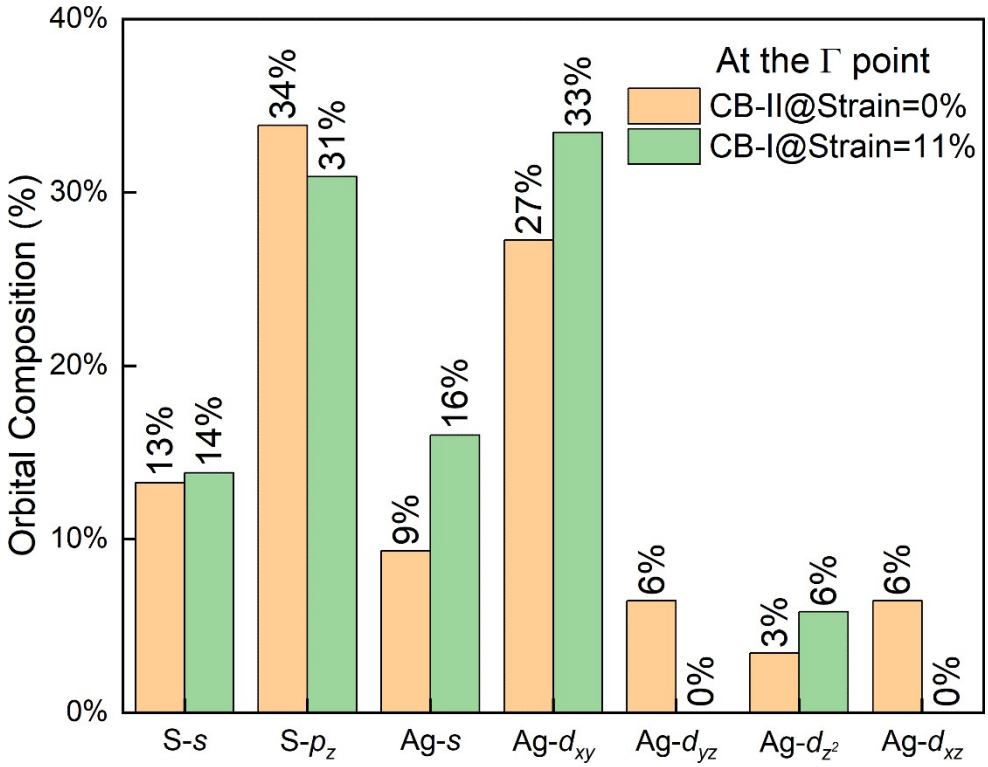

Figure S25. The orbital composition of the electronic state of CB-II of the strain-free Lieb-lattice Ag_2S and CB-I of the 11% strained Ag_2S at the Γ point.

To get a deep insight into the band switch between CB-I and CB-II at the biaxial strain of 11%, the band width of CB-I and CB-II along the Γ-X direction at the strain of 11% was first compared with that of the strain-free Ag_2S. For clarification, *original* CB-I and CB-II will respectively be used to refer to CB-I and CB-II of the strain-free Ag_2S, and CB-II and CB-I of the 11% strained Ag_2S. Upon application of a biaxial strain of 11%, the band width of original CB-I slightly decreases from 1.134 eV to 1.067 eV. This is attributed to the decrease in the overlap between the Ag-p_x, p_y orbitals which are the dominant components of original CB-I (**Figures 2c and 5b**). On the contrary, the strain of 11% leads to a significant increase in the band width of original CB-II from 0.332 eV to 0.980 eV. In order to understand such a significant increase, the orbital compositions of original CB-II at the biaxial strain of 0% and 11% are analysed. As shown in **Figure S25**, the strain of 11% only slightly changes the contribution of the S-*s* and S-p_z orbitals. In contrast, for the Ag orbitals, the Ag-d_{yz} and Ag-d_{xz} orbital components vanish at the strain of 11%, whereas the Ag-*s* and Ag-d_{xy} orbital components greatly increase. Note that the strain of 11% also substantially decreases the buckling height of Ag_2S from 2.496 Å to 1.637 Å. This may

increase the overlap/hybridization between the S-*s* orbital and the dominant Ag-*s*, d_{xy} orbitals, but weaken the hybridization between the odd-parity S-p_z orbital and the Ag-*s* and Ag-d_{xy} orbitals. Therefore, the enhanced hybridization between the S-*s* orbital and the Ag-*s*, d_{xy} orbitals and the increased composition of the latter might be responsible for the significant increase in the band width of original CB-II, and such an increase is so significant as to cause a band switch between original CB-I and original CB-II.

The edge states of the Lieb-lattice Ag_2S

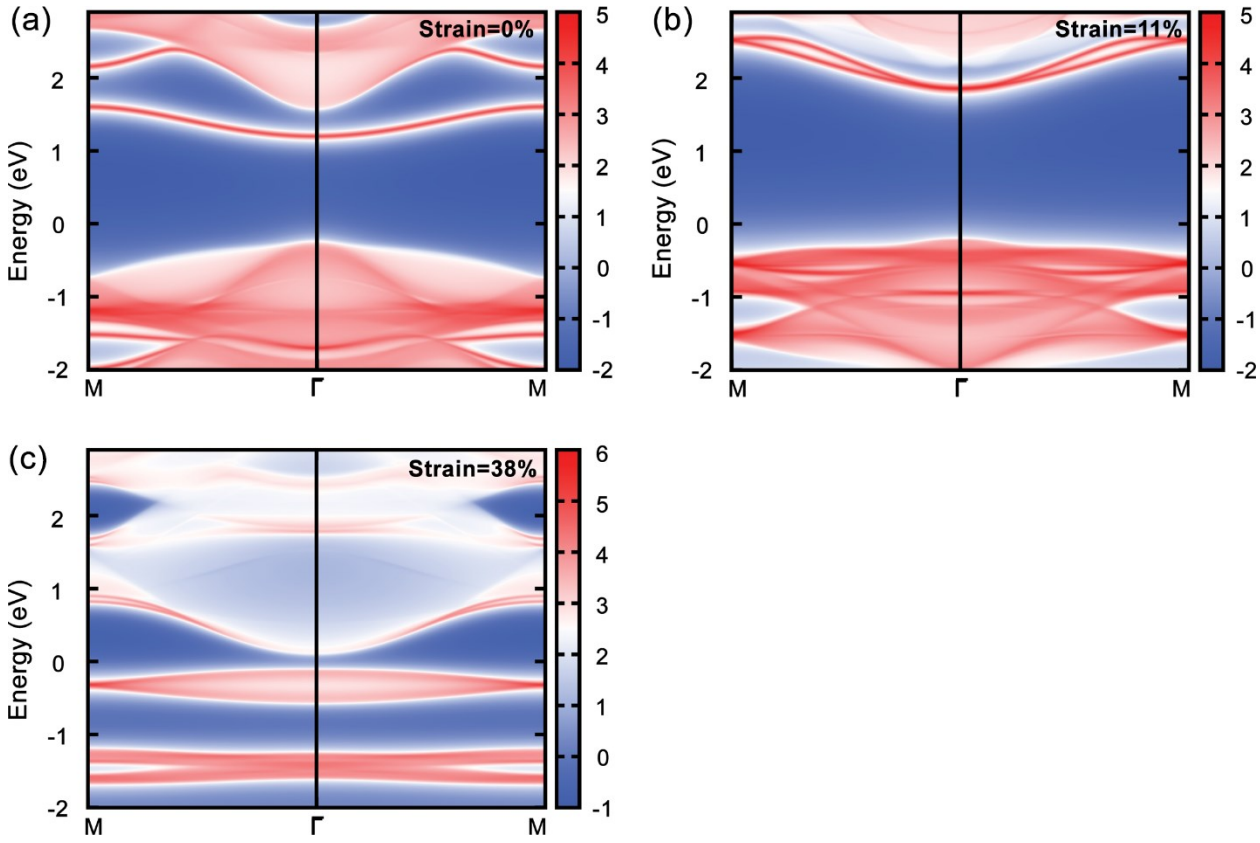

Figure S26. The edge band structure of the Lieb-lattice Ag_2S with SOC under the biaxial strain of (a) 0%, (b) 11% and (c) 38%, respectively.

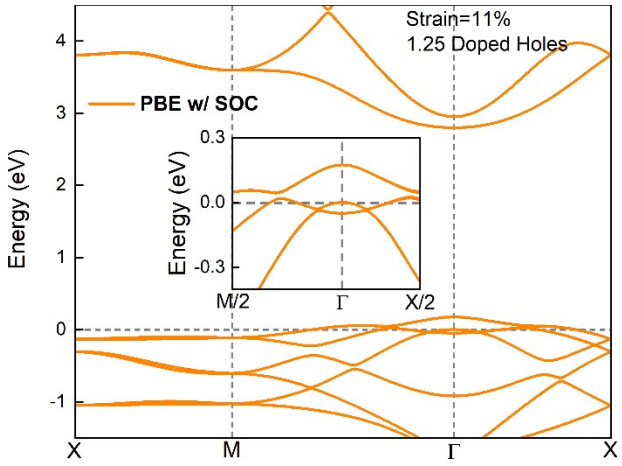

Figure S27. The electronic band structure of the 11% strained Lieb-lattice Ag_2S doped with 1.25 holes. The inset shows the zoom-in view around the valence band maximum. The horizontal dashed line denotes the Fermi level.

At the biaxial strain of 11%, VB-II and VB-III have nonzero spin Chern numbers (**Figure 5c**) and they are connected by topologically nontrivial helical edge states. As shown in **Figure S27**, the VB-II can be accessed when 1.25 holes are doped into Ag_2S.

The fitted hopping integrals in the TB model

Table S2. The fitted tight-binding model of the Lieb-lattice Ag_2S to the DFT band structure.

DFT calculation	$\epsilon_S - \epsilon_{Ag}$ **[eV]**	t_1 **[eV]**	t_2 **[eV]**	t_3 **[eV]**	t_4 **[eV]**	λ **[eV]**
PBE w/o SOC	1.843	-0.974	$0.169t_1$	$0.237t_1$	$0.364t_1$	-
PBE w/ SOC	1.763	-0.971	$0.163t_1$	$0.235t_1$	$0.361t_1$	$0.017t_1$
HSE06 w/o SOC	2.645	-1.035	$0.175t_1$	$0.233t_1$	$0.390t_1$	-
HSE06 w/ SOC	2.569	-1.122	$0.139t_1$	$0.218t_1$	$0.338t_1$	$0.016t_1$

References

1. G. Kresse and J. Hafner, *Phys. Rev. B Condens. Matter*, 1993, **48**, 13115-13118.
2. G. Kresse and J. Hafner, *Phys. Rev. B Condens. Matter*, 1993, **47**, 558-561.
3. P. E. Blöchl, *Phys. Rev. B Condens. Matter*, 1994, **50**, 17953-17979.
4. G. Kresse and D. Joubert, *Phys. Rev. B Condens. Matter*, 1999, **59**, 1758-1775.
5. J. P. Perdew, K. Burke and M. Ernzerhof, *Phys. Rev. Lett.*, 1996, **77**, 3865-3868.
6. A. Togo and I. Tanaka, *Scr. Mater*, 2015, **108**, 1-5.
7. Y. Wang, J. Lv, L. Zhu and Y. Ma, *Comput. Phys. Commun.*, 2012, **183**, 2063-2070.
8. Y. Wang, J. Lv, L. Zhu and Y. Ma, *Phys. Rev. B Condens. Matter*, 2010, **82**, 094116.
9. Y. Wang, M. Miao, J. Lv, L. Zhu, K. Yin, H. Liu and Y. Ma, *J. Chem. Phys.*, 2012, **137**, 224108.
10. A. A. Mostofi, J. R. Yates, Y.-S. Lee, I. Souza, D. Vanderbilt and N. Marzari, *Comput. Phys. Commun.*, 2008, **178**, 685-699.
11. A. A. Mostofi, J. R. Yates, G. Pizzi, Y.-S. Lee, I. Souza, D. Vanderbilt and N. Marzari, *Comput. Phys. Commun.*, 2014, **185**, 2309-2310.
12. C. L. Kane and E. J. Mele, *Phys. Rev. Lett.*, 2005, **95**, 146802.
13. M. P. L. Sancho, J. M. L. Sancho, J. M. L. Sancho and J. Rubio, *J. Phys. F: Met. Phys.*, 1985, **15**, 851-858.
14. Q. Wu, S. Zhang, H.-F. Song, M. Troyer and A. A. Soluyanov, *Comput. Phys. Commun.*, 2018, **224**, 405-416.
15. S. Grimme, S. Ehrlich and L. Goerigk, *J. Comput. Chem.*, 2011, **32**, 1456-1465.
16. S. Grimme, J. Antony, S. Ehrlich and H. Krieg, *J. Chem. Phys.*, 2010, **132**, 154104.
17. R. Peng, Y. Ma, Z. He, B. Huang, L. Kou and Y. Dai, *Nano Lett.*, 2019, **19**, 1227-1233.
18. F. Reis, G. Li, L. Dudy, M. Bauernfeind, S. Glass, W. Hanke, R. Thomale, J. Schäfer and R. Claessen, *Science*, 2017, **357**, 287-290.
19. S. Alvarez, *Dalton Trans.*, 2013, **42**, 8617-8636.
20. N. Mounet, M. Gibertini, P. Schwaller, D. Campi, A. Merkys, A. Marrazzo, T. Sohier, I. E. Castelli, A. Cepellotti, G. Pizzi and N. Marzari, *Nat. Nanotechnol.*, 2018, **13**, 246-252.
21. E. Cadelano, P. L. Palla, S. Giordano and L. Colombo, *Phys. Rev. B Condens. Matter*, 2010, **82**, 235414.
22. X. Chen, D. Wang, X. Liu, L. Li and B. Sanyal, *J. Phys. Chem. Lett.*, 2020, **11**, 2925-2933.